Analysing the Mass Structure of Small Gravitational Lens Galaxies in Galaxy Clusters

MASTERS THESIS

1st August, 2014

Wiliam Gruffydd Beynon Parry
Dark Cosmology Centre
Niels Bohr Insititute
University of Copenhagen

email: gruffp@dark-cosmology.dk

Supervisors:

CLAUDIO GRILLO (DARK Fellow)

LISE CHRISTENSEN (Assoc. Prof.)

Contents

Abstract

This thesis focuses on the estimate of the total mass of early-type galaxies, using strong gravitational lensing models, and the measurement of the luminous mass of these galaxies, using SED fitting techniques. These analyses require good photometric and spectroscopic data with which it becomes possible to explore the distribution of matter, luminous and dark, in lens galaxies.

A gravitational lens works similarly to a normal optical lens, where in the former the deflection is due to the gravitational potential of the lens. Strong lensing systems are characterised by the presence of multiple images of a single background source. The images typically surround the central main lens. The system studied in this thesis is composed of 4 multiple images of a source at $z = 2.387$ created by two lens galaxies residing in a galaxy cluster at $z = 0.352$. The available observations were taken as part of the Cluster Lensing and Supernova survey with Hubble, *CLASH*, and its spectroscopic follow-up programme at the Very Large Telescope, *CLASH-VLT*.

The total projected mass of the main lens in the system is estimated to be $M_{\mathrm{T}}(<\tilde{R}_{\mathrm{E}}) = (4.6 \pm 0.6) \times 10^{10} M_{\odot}$ with an additional 40% systematic error, where $\tilde{R}_{\mathrm{E}}$ is the Einstein radius of approximately 2.5 kpc. This corresponds to an effective velocity dispersion value of (158 ± 15) km s^{-1}, which is relatively low when compared to other strong lenses from the SLACS survey, with values ranging between 180-330 km s^{-1}. The luminous mass of the main lens is $(7.8 \pm 2.3) \times 10^{9} M_{\odot}$. A luminous over total mass fraction, projected within $\tilde{R}_{\mathrm{E}}$, was calculated to be only 0.063 ± 0.021. This value seems very low when compared to the few published studies of lens galaxies with similar luminous masses. This is of particular interest because by looking at low-mass galaxies, we can expand our knowledge about the influence of dark matter on the formation and evolution of galaxies.

The thesis will follow the following structure. Chapter 1 will introduce gravitational lensing and discuss, in detail, strong lensing theory, with focus being directed towards the description of lenses which are elliptical galaxies. In chapter 2 there will be a discussion of the general properties of elliptical galaxies and the laws which govern their structure and dynamics. An introduction of the lensing system that will be studied is done in chapter 3, followed by an estimate of the luminous masses of the two lenses found in that system and the redshifts of the lenses and the source. Chapter 4 will use strong lensing models to estimate the total mass contribution from the two lenses and attempt to disentangle their individual contributions. Chapter 5 will discuss the obtained results and estimate the luminous over total mass fraction of the main lensing galaxy and finally, chapter 6 will compare the results with other studies of this kind and discuss how this work can be expanded upon.

Chapter 1

Strong gravitational lensing

The behaviour of light as it propagates through a gravitational field is analogous to its behaviour when travelling through a lens. The deflection experienced in each case can therefore be approximated by the same set of equations, as has been thoroughly documented over the past 40 years. The propagation of light through a gravitational field is known as *gravitational lensing.* In this chapter we will discuss the theoretical framework within which strong gravitational lensing operates. It follows *Gravitational Lenses* by Schneider, Ehler and Falco[52].

1.1 History and overview

Gravitational lensing is an ever increasing field of astrophysics, ranging in application from exoplanet detection to measuring the values of the cosmological parameters of the Universe and has enabled the observations of the most distant objects in our Universe. It started in a short paper written by Albert Einstein who realised that a consequence of his General Theory of Relativity[18], GR, was that light should react to a gravitational field in the same way as massive particles do. He published a paper in 1939 [19] which outlined the foundations of the field but, unsurprisingly, failed to imagine its full scope of application when he stated, "*Of course, there is no hope of observing this phenomenon directly.*" Furthermore, Einstein only considered stars as lens candidates, unaware of the larger massive objects that could exhibit lensing properties. With the benefit of technological advancements, this phenomenon has become an increasingly important tool within astrophysics over the last 20 years.

The breakthrough occurred in 1979 when the first strong gravitational lens was found by Walsh, Carswell and Weymann[59], who observed two multiple images of a distant quasar produced by the gravitational field of a foreground lens galaxy shown in Fig. 1.1.1.

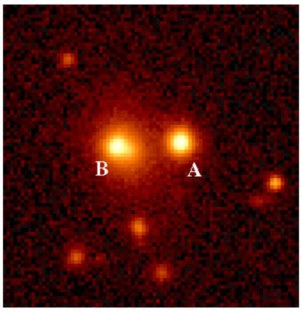

Figure 1.1.1: The first confirmed lensed images of a quasar observed by Walsh, Carswell and Weymann in 1979[59]. A and B are images of a single, distant quasar (quasar 0957+561) created by a foreground massive object which cannot be seen in the figure.

Gravitational lensing operates in three regimes: the weak-, micro- and strong-lensing regimes. Weak lensing manifests itself as a small amount of distortion in the shape of a source galaxy. An observation of a single galaxy does not provide sufficient information to determine whether or not the shape of the galaxy is its true shape or if the light has been distorted whilst travelling to the observer. As a consequence, weak-lensing can only be detected statistically with a large data set and has been used to infer the dark matter distribution in the outer regions of galaxies[26, 57] and galaxy clusters[22, 9].

Microlensing is observed as a magnification in a source. An area where it plays an important role is in the detection of exoplanets, where an amplification in a source star's luminosity is observed as a foreground star passes between source and observer[2]. If the foreground star has a planet orbiting it then the lightcurve exhibits an a-symmetric peak, as can be seen in Fig. 1.1.2.

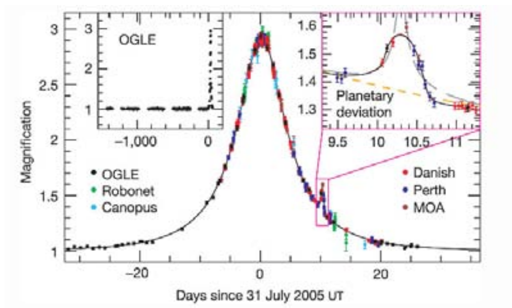

Figure 1.1.2: The figure shows the light curve of the OGLE-2005-BLG-390 microlensing event[2]. The top left inset shows the OGLE light curve extending over the previous 4 years. The top right inset is a close-up look at the microlensing caused by a planet orbiting the main lens.

This paper will focus on the third regime of gravitational lensing, strong lensing. Strong lensing is similar to microlensing but they differ in scale. In microlensing the images are unresolved and the lightcurve is analysed to infer the presence of lensing, but with strong lensing the light from the source bends in the presence of a gravitational field to such an extent that multiple images of said source can be observed. The measurements that are obtainable from these observations have had many profound implications on the field of astrophysics. Firstly, due to the

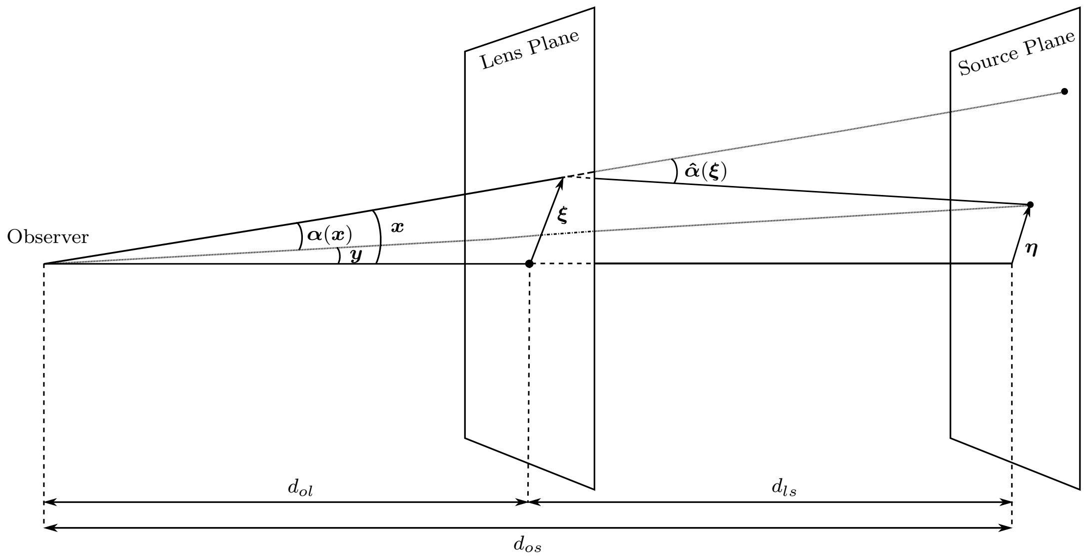

Figure 1.2.1: A diagram showing the geometric configuration of a typical lensing system illustrating the effect of the gravitational potential on the path of a photon. The photon is emitted form a source at a distance d_{os} from the observer and then deflected by the gravitational potential of a lens at distance d_{ol} from the observer. The lens could be a planet, star, galaxy, galaxy cluster, any object that has mass, dark matter or ordinary matter.

magnification effect of gravitational lensing, very distant objects are now within our observational limit which let us peer at objects in with large redshifts[46, 62, 61]. This provides us with a far deeper understanding of the formation and evolution of objects in the early Universe. Secondly, the time delays of beams of light emitted from a single source, as a result of their differing paths through the gravitational potential of the lens, puts constraints on the fundamental cosmological parameters of the Universe[56]. Lastly, very accurate measurements of the total mass of the lensing galaxies are obtainable[37, 29]. When these measurements are compared to those obtained through analysis of the lens galaxy's luminosity profile, the total mass can be decomposed into its luminous and dark matter components.

1.2 Theory

The Universe is well described by the Friedmann-Lemaître-Robertson-Walker[25, 39, 47, 58] metric wherein observed lensing effects are a result of gravitational potentials local to the lens and there are no perturbations in the region between observer and lens, d_{ol}, and between lens and source, d_{ls}. According to GR and in the limit of a weak field, $\Phi = GM/\xi << c^2$, were G, c and ξ are Newton's constant of gravity, the velocity of light in vacuum and the impact parameter, respectively, the deflection of a beam of light as it passes a lens of mass M is given by

$$\hat{\alpha} = \frac{4GM}{c^2\xi}. \tag{1.1}$$

We can immediately test whether or not we are in a weak field by considering the typical observed velocity dispersions for elliptical galaxies. A galaxy's gravitational potential, Φ, and its velocity dispersion, σ_v are related through,$\Phi \sim {\sigma_v}^2$ when in virial equilibrium. In massive elliptical galaxies we get measurements of σ_v in the range of 200-400 km s^{-1}[5], and therefore$\Phi \sim \sigma_v^2 \sim (400\text{km s}^{-1})^2 << c^2$.

GR states that light rays travel along null geodesics and any deflection is a consequence of the curvature of space-time itself. Thus, during these deflections there is no emission or absorption of radiation so the surface brightness of distant sources is conserved throughout their journey through gravitational potentials.

1.2.1 The lens equation

As shown in Fig. 1.2.1, light travelling from a source to an observer via a lens is deflected at the lens plane. This deflection results in an apparent position of the source which differs from the true position. These positions are typically measured from the central axis position, defined as being a straight line between the observer and the centre of the lens which is extended to the source plane. To derive the equation governing the path that the beam of light takes through the lens we return to Fig. 1.2.1. The position vector of the source in the absence of a lens is given by $\boldsymbol{\eta}$, $\boldsymbol{y}$ in angular position, and the position vector of the source as seen on the lens plane, which has been deflected by a lens, is given by $\boldsymbol{\xi}$, $\boldsymbol{x}$ in angular position, all in relation to the centre of their respective planes.

When the typical diameter of a galaxy, 1-30 kpc, is compared to the observer-lens distance, d_{ol}, and the lens-source distance, d_{ls}, which are $\sim$ 1 Gpc, it is evident that a thin lens approximation is sufficient in describing the properties of the lens. The impact of this is that any individual mass components the galaxy has can be projected onto a single plane, with a continuous projected surface mass density along the line of sight of$\Sigma(\boldsymbol{\xi}) := \int dr_3 \rho(\xi_1, \xi_2, r_3)$, where ρ is the 3D density.

The weak field approximation suggests that we are working with small deflections and therefore the small angle approximation, $\sin\alpha \approx \tan\alpha \approx \alpha$, can be used to give us the geometric relations

$$\boldsymbol{\xi} = d_{ol}\boldsymbol{x}, \quad \boldsymbol{\eta} = d_{os}\boldsymbol{y} \tag{1.2}$$

With some simple trigonometric manipulation

$$\boldsymbol{\eta} = \boldsymbol{x} d_{os} - \hat{\boldsymbol{\alpha}}(\boldsymbol{\xi}) d_{ls} \tag{1.3}$$

$$\boldsymbol{y} = \boldsymbol{x} - \frac{d_{ls}}{d_{os}} \hat{\boldsymbol{\alpha}}(d_{ol}\boldsymbol{x}) = \boldsymbol{x} - \boldsymbol{\alpha}(\boldsymbol{x}) \tag{1.4}$$

we can arrive at the ray-tracing equation or the *lens equation*, Eq. (1.4). This relates the true position of a source, $\boldsymbol{y}$, to the apparent position of the source as seen by an observer, $\boldsymbol{x}$.

Another consequence of the weak gravitational field approximation is that the deflections caused by the individual mass components on the lens plane can be linearised and thus

$$\hat{\boldsymbol{\alpha}}(\boldsymbol{\xi}) = \sum_i \hat{\boldsymbol{\alpha}}_i(\boldsymbol{\xi}) = \frac{4G}{c^2} \sum_i M_i \frac{\boldsymbol{\xi} - \boldsymbol{\xi}_i}{||\boldsymbol{\xi} - \boldsymbol{\xi}_i||^2} \tag{1.5}$$

where $\boldsymbol{\xi} - \boldsymbol{\xi}'/||\boldsymbol{\xi} - \boldsymbol{\xi}'||$ was used to define the direction of the deflection due to the individual mass components. Replacing the discrete mass distribution with a continuous one and projecting it onto the lens plane gives us the deflection angle in integral form

$$\hat{\boldsymbol{\alpha}}(\boldsymbol{\xi}) = \frac{4G}{c^2} \int d^2\xi' \Sigma(\boldsymbol{\xi}') \frac{\boldsymbol{\xi} - \boldsymbol{\xi}'}{||\boldsymbol{\xi} - \boldsymbol{\xi}'||^2} \tag{1.6}$$

If we would like to calculate the scaled deflection angle, $\boldsymbol{\alpha}(\boldsymbol{\xi})$ see Eq. (1.4), instead of the deflection angle, $\hat{\boldsymbol{\alpha}}(\boldsymbol{\xi})$, we would first need to define a dimensionless surface mass density, which is also known as the *convergence*,

$$\kappa(\boldsymbol{x}) := \frac{\Sigma(\boldsymbol{x})}{\Sigma_c} \tag{1.7}$$

whereΣ_c is the critical surface mass density, defined as

$$\Sigma_c := \frac{c^2}{4\pi G} \frac{d_{os}}{d_{ol} d_{ls}} \tag{1.8}$$

The critical surface mass density is not an intrinsic property of a lens, but rather it relies on the geometry of the observer-lens-source. An estimate of the convergence can be translated into a measurement of the mass of a lens, as will be seen later in this chapter. We can now write the scaled deflection angle as

$$\boldsymbol{\alpha}(\boldsymbol{x}) = \frac{1}{\pi}\int d^2x'\kappa(\boldsymbol{x}')\frac{\boldsymbol{x}-\boldsymbol{x'}}{||\boldsymbol{x}-\boldsymbol{x'}||^2} \tag{1.9}$$

Here, we can also introduce the deflection potential, ψ, which will be useful when discussing some of the properties of the images produced in a strong lens system

$$\psi(\boldsymbol{x}) := \frac{1}{\pi}\int \kappa(\boldsymbol{x}')\ln||\boldsymbol{x}-\boldsymbol{x}'||\mathrm{d}^2x' \tag{1.10}$$

and so it follows that

$$\boldsymbol{\alpha}(\boldsymbol{x}) = \nabla_{\boldsymbol{x}}\psi(\boldsymbol{x}), \tag{1.11}$$

where the identity $\nabla_{\boldsymbol{x}}\ln||\boldsymbol{x}|| = \boldsymbol{x}/||\boldsymbol{x}||^2$ was used. We can also use Eq. (1.10) using the identity$\Delta\ _{\boldsymbol{x}}\ln||\boldsymbol{x}|| = 2\pi\delta(\boldsymbol{x})$ to to get the lensing potential in terms of the convergence

$$\Delta_{\boldsymbol{x}}\psi(\boldsymbol{x}) = 2\kappa(\boldsymbol{x}) \tag{1.12}$$

where $\delta(\boldsymbol{x})$ is the two-dimensional delta-function and $\Delta_{\boldsymbol{x}}$ is the Laplacian with respect to $\boldsymbol{x}$.

1.2.2 Magnification and distortion

It is not only the change in position that we need to consider when discussing lensing theory, but also the distortion that might occur to the image of a source during transformation through the lens equation. Lensing conserves the surface brightness of a source which is lensed, as discussed earlier. However, the solid angle,$\Delta\ \omega$, that the source subtends on the sky is not conserved. As such, one could describe a source as being magnified if the solid angle of the image of the source on the lens plane is larger than that of the same source were it not lensed. In relation to the lensing equation, the amount of distortion is given by the determinant of the Jacobian matrix of the lens mapping $\boldsymbol{x} \rightarrow \boldsymbol{y}$

$$A_{ij}(\boldsymbol{x}) = \frac{\partial \boldsymbol{y}_i}{\partial \boldsymbol{x}^j} \tag{1.13}$$

where i and j are the indices of a 2x2 matrix. This only holds true when used locally, where the properties of the lens do not change considerably. Applying the lens equation, Eq. (1.4), gives

$$A_{ij}(\boldsymbol{x}) = \delta_{ij} - \frac{\partial \boldsymbol{\alpha}_i(\boldsymbol{x})}{\partial \boldsymbol{x}^j} \tag{1.14}$$

$$\text{Eq. (1.11)} \Rightarrow A_{ij}(\boldsymbol{x}) = \delta_{ij} - \psi_{,ij}(\boldsymbol{x}) \tag{1.15}$$

where the comma-derivative notation is used: $\psi_{,ij} = \partial^2\psi/\partial\boldsymbol{x}^i\partial\boldsymbol{x}^j$. The Jacobian matrix can be explicitly written as

$$A_{ij}(\boldsymbol{x}) = \begin{pmatrix} 1-\kappa(\boldsymbol{x})-\gamma_1(\boldsymbol{x}) & -\gamma_2(\boldsymbol{x}) \\ -\gamma_2(\boldsymbol{x}) & 1-\kappa(\boldsymbol{x})+\gamma_1(\boldsymbol{x}) \end{pmatrix}. \tag{1.16}$$

Here, the elements of A are expressed in terms of two quantities, convergence and shear, $\gamma(\boldsymbol{x})$. The shear distorts the shape of the source and can be split into two components, γ_1 and γ_2. In terms of the lensing potential the shear components are

$$\gamma_1 = \frac{1}{2}(\psi_{,11} - \psi_{,22}) \tag{1.17}$$

$$\gamma_2 = \psi_{,12} = \psi_{,21} \tag{1.18}$$

From Eq. (1.16) we can see that the Jacobian matrix, A, is symmetric and has eigenvalues corresponding to $1-\kappa(\boldsymbol{x}) \pm \gamma(\boldsymbol{x})$.

A lens distorts an area element around $\boldsymbol{y}$ into one around $\boldsymbol{x}$. The change in area is known as the magnification, $\mu(\boldsymbol{x})$. In order to estimate the magnification, we need to take the inverse of the determinant of the Jacobian matrix

$$\mu(\boldsymbol{x}) = \frac{1}{\det A(\boldsymbol{x})} \tag{1.19}$$

The absolute value of $\mu(\boldsymbol{x})$, μ, describes the ratio of the size of an image in relation to the corresponding source, where an image with $\mu > 1$ is considered magnified and with $\mu < 1$ considered demagnified. The sign of $\mu(\boldsymbol{x})$ tells us the parity of the image, where a negative value means that there has been a mirror-symmetric transformation of the image with respect to the source.

From Eq. (1.16) we can express the magnification as

$$\mu(\boldsymbol{x}) = \frac{1}{\det A(\boldsymbol{x})} = \frac{1}{(1-\kappa(\boldsymbol{x}))^2 - \gamma^2(\boldsymbol{x})} \tag{1.20}$$

1.2.3 Critical curves and caustics

Regions of the lens plane can have a positive or negative value of the magnification. One can imagine that there exists a position on the lens plane where the sign of μ flips, and the value of $\det A$ is temporarily 0. At this point, as a consequence of Eq. (1.19), the magnification diverges and would be infinite. The magnification of an astrophysical object in fact stays finite since the source is never a true point source. The region of the lens plane where $\det A = 0$ is important as it defines what is known as the *critical curves.* Critical curves are smooth, closed curves and are defined as the points on the lens plane where $\det A(\boldsymbol{x}) = 0$. By mapping these curves through the lens equation onto the source plane we obtain the so-called *caustics*, which can be smooth or develop cusps. With a given position of observer and lens, the number of multiple images depends on the position of a source with respect to the caustics. On one side of a caustic a source will be observed with a certain number of multiple images on the lens plane, on the other side of the caustic it will be observed with a different number of images on the lens plane, either by an increase or decrease of 2. As the source passes the caustic, two multiple images of that source are either created or merged. We will define the region of a caustic corresponding to fewer images as being "outside" and the region corresponding to more images as being the "inside".

It is the geometry of the lens and its mass distribution, as well as the relative distances between observer and lens and between lens and source, which determine the positions and shapes of these critical curves and caustics.

1.3 Lens models

1.3.1 Circular lenses

Due to the symmetry of a circular lens, we only need to consider radial distances $||\boldsymbol{x}|| = x$ and thus the surface mass density can be expressed as $\Sigma(\boldsymbol{x}) = \Sigma(x)$. In such a situation, any and all images of a source seen on the lens plane are found to lie on a line passing through the source and the centre of the lens, with the exception of when the observer, source and lens centre are collinear where an image of a ring is formed.

Consider the scaled deflection angle, Eq. (1.9), when we insist that $\boldsymbol{x}$ lies on the positive x_1 axis, i.e. $\boldsymbol{x} = (x, 0)$, and neglect the situation where $x = 0$ for the time being, so that $x > 0$. In polar coordinates, $\boldsymbol{x}' = x'(\cos\theta, \sin\theta)$ and using $d^2x' = x'dx'd\theta$ we find that

$$\alpha_1(\boldsymbol{x}) = \frac{1}{\pi}\int_0^\infty x'dx'\kappa(x')\int_0^{2\pi} d\theta \frac{x - x'\cos\theta}{x^2 + x'^2 - 2xx'\cos\theta} \tag{1.21a}$$

$$\alpha_2(\boldsymbol{x}) = \frac{1}{\pi}\int_0^\infty x'dx'\kappa(x')\int_0^{2\pi} d\theta \frac{-x'\sin\theta}{x^2 + x'^2 - 2xx'\cos\theta}. \tag{1.21b}$$

It can be shown that Eq. (1.21b) vanishes due to symmetry

$$\begin{aligned}\alpha_2(\boldsymbol{x}) &= \frac{1}{\pi}\int_0^\infty x'dx'\kappa(x')\int_0^{2\pi} d\theta \frac{-x'\sin\theta}{x^2 + x'^2 - 2xx'\cos\theta} \\ &= \frac{1}{\pi}\int_0^\infty x'dx'\kappa(x')\left[-\frac{\ln(x^2 + x'^2 - 2xx'\cos\theta)}{x}\right]_0^{2\pi} = 0\end{aligned} \tag{1.22}$$

suggesting that $\boldsymbol{\alpha}$ is parallel to $\boldsymbol{x}$. The inner integral of Eq. (1.21a) reduces to $2\pi/x$

$$\begin{aligned}\alpha_1(\boldsymbol{x}) &= \frac{1}{\pi}\int_0^\infty x'dx'\kappa(x')\int_0^{2\pi} d\theta \frac{x - x'\cos\theta}{x^2 + x'^2 - 2xx'\cos\theta} \\ &= \frac{1}{\pi}\int_0^\infty x'dx'\kappa(x')\left[\frac{\frac{2x'^2\tanh^{-1}\left[\frac{(x^2+xx'+x'^2)\tan\left(\frac{\theta}{2}\right)}{\sqrt{-x^4-x^2x'^2-x'^4}}\right]}{\sqrt{-x^4-x^2x'^2-x'^4}} + \theta}{x}\right]_0^{2\pi} \\ &= \frac{2}{x}\int_0^\infty x'dx'\kappa(x')\end{aligned} \tag{1.23}$$

It should also be noted that when $x' > x$, there is no further contribution to the deflection angle whereas when $x' < x$ there is a contribution to the deflection angle, analogous to the way gravitational forces of spherical mass distributions behave. This allow us to express the deflection angle as

$$\alpha(x) = \alpha_1(x) = \frac{2}{x}\int_0^x x' dx' \kappa(x') := \frac{m(x)}{x} \tag{1.24}$$

where $m(x)$ is the dimensionless mass within a circle of radius x.

It follows that the mean surface mass density, $\langle\kappa(x)\rangle$, within a circle of radius x is

$$\langle\kappa(x)\rangle := \frac{m(x)}{x^2}, \tag{1.25}$$

so we can re-write the lens equation as

$$\boldsymbol{y} = \boldsymbol{x}[1 - \langle\kappa(x)\rangle]. \tag{1.26}$$

From this version of the lens equation we can define the typical length scale of a strong lens, R_{E}, also known as the Einstein radius. For all points, $\boldsymbol{x}$, which satisfy the condition $\langle\kappa(x)\rangle = 1$, i.e. the enclosed mean surface mass density is equal to the critical surface mass density, $\boldsymbol{y} = 0$. Here, all points x sit on a ring whose radius is used to define R_{E}. It is therefore possible to estimate the mass enclosed within this ring as

$$M(\leq R_{\mathrm{E}}) = \Sigma_c \pi R_{\mathrm{E}}^2. \tag{1.27}$$

It is rare that a source and a lens are collinear and that we have a perfectly spherically symmetric lens, therefore the observed Einstein rings are almost never perfect. Fig. 1.3.1 shows some good examples of these rings.

In the circularly-symmetric case and from Eq. (1.16), $\det A$ can be written as

$$\det A(\boldsymbol{x}) = \frac{y}{x}\frac{dy}{dx} = \left(1 - \frac{\alpha(x)}{x}\right)\left(1 - \frac{\mathrm{d}}{\mathrm{d}x}\alpha(x)\right) \tag{1.28}$$

From our definition of critical curves as being the curves where $\det A(\boldsymbol{x}) = 0$, we can see that there must be two kinds of critical curves, one where $\alpha(x)/x = 1$ and one where $\frac{d}{dx}\alpha(x) = 1$. These critical curves are called a *tangential critical curve*

Figure 1.3.1: Examples of observed Einstein rings. Courtesy of NASA, ESA, A. Bolton (Harvard-Smithsonian CfA), and the SLACS Team.

and a *radial critical curve*, respectively. The tangential critical curve is mapped into $y = 0$ through the lens equation and so a circular lens has a tangential caustic which is a single point at the source plane centre.

We now consider different density profiles, $\rho(r) \propto r^{-n}$, in the circular lens case, as discussed by Evans and Wilkinson (1998)[20] and part 2 of *Gravitational Lensing: Strong, Weak and Micro* by C.S. Kochanek (2004)[53]. The scaled deflection angle becomes

$$\alpha(x) = b\left(\frac{x}{b}\right)^{2-n}, \tag{1.29}$$

where b can be thought of as a lens strength of which the definition depends on the model in question, as will be discussed further on on this section. The convergence and shear profiles become

$$\kappa(x) = \frac{3-n}{2}\left(\frac{x}{b}\right)^{1-n} \tag{1.30}$$
$$\gamma(x) = \frac{n-1}{2}\left(\frac{x}{b}\right)^{1-n} \tag{1.31}$$

and the radial and tangential eigenvalues of these models become

$$1-\kappa(x)+\gamma(x) = 1-\frac{\mathrm{d}\alpha(x)}{\mathrm{d}x} = 1-(2-n)\left(\frac{x}{b}\right)^{1-n} \tag{1.32a}$$
$$1-\kappa(x)-\gamma(x) = 1-\frac{\alpha(x)}{x} = 1-\langle\kappa(x)\rangle = 1-\left(\frac{x}{b}\right)^{1-n} \tag{1.32b}$$

These *power-law* profiles cover the models which are most used to represent the profiles of galaxies. The simplest model is a point mass, M, which is commonly used as an approximation in microlensing. It has an index, $n = 3$ and produces a

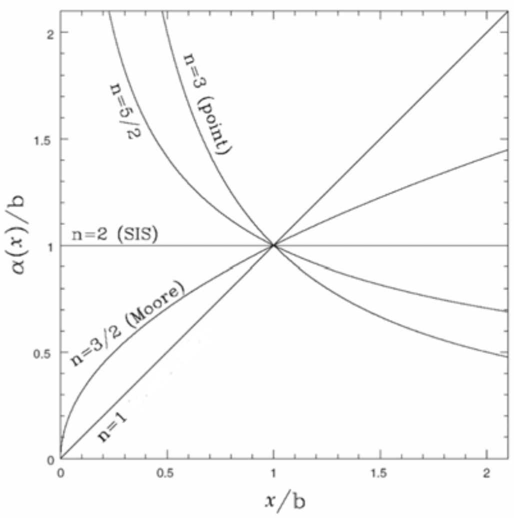

Figure 1.3.2: The deflection angles scaled to the lens strength b for differing indices, n[53].

deflection of $\alpha(x) = b^2/x$, with convergence $\kappa(x) = 0$ and shear $\gamma(x) = b^2/x^2$. A good starting point for strong-lensing models is a profile where $n = 2$, known as a Singular Isothermal Sphere, SIS. From Eq. (1.29) it can be seen that the deflection angle here is is equal to the lens strength and Eq. (1.30) and (1.31) show that $\kappa(x) = \gamma(x) = b/2x$. The $n = 1$ power law model describes a uniform critical sheet where $\alpha(x) = x$, $\kappa(x) = 1$ and $\gamma(x) = 0$. This model can be thought of as only having a contribution when $y = 0$. At this point, an infinitely bright plane is produced on the lens plane, at any point where $y \neq 0$ no image is observed on the lens plane. Other models can be used to account for various other problems encountered, e.g. the inner cusp of the mass distribution can be modelled using a power index of $n = 3/2$, known as the Moore profile[41].

Fig. 1.3.2 shows the deflection angles scaled to the lens strength b for differing indices, n. The lens strength, as mentioned earlier, depends on the model being used and it is the best-estimated parameter in lens modelling, since it is effectively the deflection angle.

We define the tangential critical curve by observing from Eq. (1.32b) that the tangential eigenvalue is equal to zero at $x = b \equiv \theta_E$. It creates the circle that we encountered earlier in this chapter defined as the Einstein ring and is equivalent to the tangential critical curve. Within the tangential critical radius $\langle\kappa(x)\rangle \equiv 1$, independent of the model, i.e. independent of the value of n. Once angular structure is applied, as it will be done later in this chapter, this is no longer strictly true but it is still a good approximation.

Singular Isothermal Sphere, SIS

One can assume that the stars of a galaxy behave like the particles of an ideal gas, confined by a spherically symmetric gravitational potential. This can give us a simple model which has an equation of state

$$p = \frac{\rho k T}{m} \tag{1.33}$$

where ρ, m and T are the density, mass and temperature of a galaxy, respectively, and k is Boltzmanns constant. In thermal equilibrium $m\sigma_v^2 = kT$. In a SIS, the temperature is assumed constant, i.e. the stellar gas is isothermal and hence the velocity dispersion is also constant. Using the equation of hydrostatic equilibrium we can show that the density distribution for a SIS model is given by

$$\rho(r) = \frac{\sigma_v^2}{2\pi G r^2}. \tag{1.34}$$

The Singular aspect of the model arises as a consequence the fact that the density, $\rho(r)$, diverges as $r \to 0$. Hence great care must be taken when modelling the inner most region.

Observations have shown that spiral galaxies have flat rotation curves[48], out to large radii. This means that in their outer regions, the cumulative total mass increases proportional to r and therefore a total density distribution similar to that presented above is appropriate to describe this class of objects. The same density distribution has also been shown to describes well the lensing properties of galaxies[4] and galaxy clusters[63]. When modelling the outer most region, $r \to \infty$, the total mass of a SIS diverges. Typically, a truncation radius is chosen to keep the mass finite.

The surface mass density,$\Sigma($ $R)$ of a SIS is given by projecting the three dimensional density distribution, $\rho(r)$, along the line-of-sight

$$\Sigma(R) = 2\int_R^\infty \rho(r)\frac{r}{\sqrt{r^2 - R^2}}\mathrm{d}r = \frac{\sigma_v^2}{2GR}$$

allowing us to obtain the mass within a radius R for a SIS,

$$M(R) = 2\pi \int_0^R R'\Sigma(R')\mathrm{d}R' = \frac{\pi\sigma_v^2 R}{G}. \tag{1.35}$$

Eq. (1.1) leads to an expression for the deflection angle in terms of the velocity dispersion,

$$\hat{\alpha}(\xi) = 4\pi\left(\frac{\sigma_v}{c}\right)^2, \tag{1.36}$$

and the lens equation, Eq. (1.4), allows us to find the scaled deflection angle,

$$\alpha(x) = 4\pi\left(\frac{\sigma_v}{c}\right)^2 \frac{d_{ls}}{d_{os}} = \theta_{\mathrm{E}}. \tag{1.37}$$

From this we can see that the scaled deflection angle of a SIS does not depend on x and is equal to the Einstein radius. Using Eq. (1.26) we can recover the expression for the $n = 2$ model discussed earlier

$$\kappa(x) = \frac{\theta_E}{2|x|} \tag{1.38}$$

The SIS model produces two images if $0 < y < \theta_{\mathrm{E}}$, i.e. the source lies within the tangential caustic on the source plane. One of these images is a located outside of θ_{E} at $x_1 = y + \theta_{\mathrm{E}}$ with a positive magnification, $\mu_1 = 1 + \theta_{\mathrm{E}}/y$, and the other image is located inside θ_{E} but on the opposite side of the lens, $x_2 = y - \theta_{\mathrm{E}}$, i.e. $-\theta_{\mathrm{E}} < x_2 < 0$, with a negative magnification, $\mu_2 = 1 - \theta_{\mathrm{E}}/y$. The separation between the two images is constant, $|x_1 - x_2| = 2\theta_{\mathrm{E}}$. Any source that lies outside of the radial caustic will only produce one image.

1.3.2 Non-circular lenses

In most cases the angular structure of a lens cannot be neglected. There are two factors to take into account: the ellipticity of a galaxy's total matter distribution and perturbations that arise from external objects which might be in the vicinity of the lens, either in projection or along the line of sight.

It has been shown that the dark matter distribution of galaxies closely matches that of the luminous mass[37]. This simplifies the scenario, at least to the accuracy of available observational confirmation. A SIS is generalised to a Single Isothermal Ellipsoid, SIE, where all the relevant lensing quantities can be expressed as a function of an elliptical radius, $\zeta = \sqrt{q^2\xi_1^2 + \xi_2^2}$, where q is the axis ratio.

The contribution from objects which are not included in the main lens model can be accounted for by using an external shear component, γ, or by adding additional lenses to the model. It is clear that it is not ideal to keep adding mass components in order to best replicate the observed positions of sources, and so every addition to a model must be done carefully and its effect on the overall model's physical validity must be considered.

Chapter 2

Elliptical galaxies, an overview

This chapter will discuss the structure and kinematics of galaxies, where focus will be directed at elliptical galaxies because this class of galaxies will also be studied in later chapters. A brief overview of galaxy classification and morphology will be given before discussing the physical quantities which are used to describe their dynamical structure, formation history and photometry. The end of this chapter will be a small section on Dark Matter, DM.

2.1 Galaxies - history and classification

Galaxy classification began when Edwin Hubble speculated on the evolution of a galaxy. From his observations, he surmised that galaxies evolved in accordance to his famous *tuning fork* diagram, shown in Fig. 2.1.1. Hubble believed that all galaxies began as ellipticals and then evolved to being spiral galaxies. This is not the currently agreed upon model for galaxy evolution, but the terminology used to describe the model is still used in modern astrophysics and astronomy. Elliptical, E, galaxies as well as lenticular, S0, galaxies are referred to as *Early-Type* Galaxies, ETGs, whereas spiral galaxies are referred to as *Late-Type* Galaxies, LTGs. According to the Hubble Morphological Classification, all ETGs are labelled with an E followed by a number characterising the ellipticity of the galaxy, with a larger number representing a more elongated galaxy. Users of this classification system should be aware that the ellipticity here is the *apparent* ellipticity, the projection of a galaxy's shape along our line of sight, as seen on the celestial sphere. LTGs are characterised by the presence, or lack of a central bar, denoted

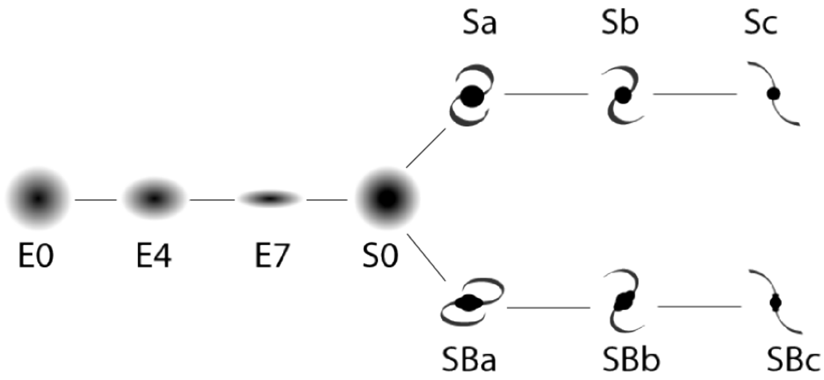

Figure 2.1.1: The tuning fork diagram proposed by Edwin Hubble as a viable evolutionary representation of galaxies. Despite the fact that this idea is considered incorrect in modern astronomy and astrophysics, the terminology coined by Edwin Hubble is still used today when classifying galaxies. Image obtained from the University of Michigan Astronomy Department[40]

by a B, and by the tightness of their spiral arms, denoted by either an a, b or c. An Sa galaxy is a spiral galaxy with tightly wound spiral arms and no central bar, whereas an SBc galaxy has more defined spiral arms and a central bar is present.

In later chapters, a system will be introduced which has a large elliptical galaxy acting as a lens, and it is for this reason that the discussion will be directed towards "normal" ETGs, which include giant ellipticals, intermediate ellipticals, and compact ellipticals. In the study of gravitational lens, more attention has been given to ETGs because they outnumber LTGs at masses greater than $3 \times 10^{10} M_{\odot}$. Observed lenses have a bias towards large masses and consequently, a bias towards being ETGs.

2.2 Early-type galaxies, ETGs

ETGs range in scale, $1 - 100$ kpc, and total mass, $10^{9} - 10^{13} M_{\odot}$, and appear mostly red when observed in the optical bands. This red colour indicates that they consist of older stellar populations, whereas LTEs are bluer and are thought to be rich in star forming regions and have a stellar population consisting of both old and young stars. The stars within an ETGs are characterised by their large peculiar motion, where the velocity of a star through the galaxy is more random, when compared to LTEs which have a very ordered rotation. This peculiar motion suggests that ETGs are predominantly pressure supported.

2.2.1 The formation of ETGs

One model for the formation of ETGs is one where gas found within a Dark Matter, DM, halo instantaneously transforms into stars, this formation model is known as the *monolithic collapse*. Even though this simple model explains the observed high velocity dispersion of the stars within ETGs, it does not suggest a mechanism for this instantaneous star formation.

Another, more popular, formation mechanism is one of hierarchical structure formation, where large galaxies form from the merging of smaller galaxies or gas clouds. These mergers can be called minor if one of the merging galaxies is significantly smaller than the other. In the *minor merger* scenario, the large-scale structure of the large galaxy is unaffected and the stellar components of the smaller galaxy is simply added to the larger galaxy's stellar population. The minor merger scenario, while likely to be occurring, is insufficient to explain the origin of an ETG and the large velocity dispersion of the stars. A merger can be considered major if the merging galaxies are of comparable size. In the *major merger* scenario, the properties of a galaxy can change completely. Imagine the merging of two spiral galaxies of comparable mass. From either galaxy's frame of reference, the introduction of a large mass object would destroy their respective discs and the stars would be thrown into new trajectories. Some stars and gas would be ejected completely, while the rest would simply find new stable orbits.

The major merger scenario is able to account for the large velocity dispersion, as does the monolithic collapse, but it does not invoke a new star formation mechanism and has therefore been widely used as the formation mechanism of ETGs. The main problem facing this model is in explaining the "redness" of ETGs which were formed at low redshifts, since the merging of the gas components of two galaxies is expected to trigger star formation. A possible explanation to this is to consider mergers where star formation is not triggered, ones where the two galaxies are gas-poor. In the case where two gas-rich galaxies merge, star formation is triggered, whereas two gas-poor galaxies would not significant increase the global star formation rate. These are known as "wet" and "dry" mergers, respectively.

2.2.2 The structure and dynamics of ETGs

Most ETGs are dominated by an old stellar population, giving rise to their characteristic red colour. They contain a small amount of gas, relative to LTGs, shown by their X-ray emission from hot gas[23], the presence of Hα emission lines from warm gas[45] and a small amount of cold gas detected from HI[36] and CO[35] molecular lines. A galaxy's formation history dictates the amount of star forming regions, as discuss above, or whether or not a Super Massive Black Hole, SMBH, is present at the centre. The presence of SMBHs can be observed in the X-ray emission from an accretion disk which surrounds it.

The dynamical structure of ETGs have no preferred direction of motion. It is for this reason that ETGs are considered featureless spheroidal galaxies, which are pressure supported. The two-body relaxation time is given by

$$\tau_{\mathrm{r}} \sim \frac{\sigma^3}{G^2 m^2 n \log\Lambda}, \tag{2.1}$$

where σ is a typical velocity dispersion, G is the Newtonian gravitational constant, m is the typical mass of a star, n is the number of stars per unit volume and $\log\Lambda$ is the Coulomb logarithm, which is the ratio of small angle collisions to large angle collisions. For an ETG, $\tau_{\mathrm{r}} \sim 10^{14}$ years, which is much higher than the Hubble time and therefore elliptical galaxies can be considered collision-less systems. The relaxation time is less in the core and so we expect the inner regions to be in equilibrium but sufficient time is yet to pass for the outer regions to experience sufficient phase-mixing to reach equilibrium.

2.3 Modelling elliptical galaxies

2.3.1 The luminosity profile

Modelling the luminosity profile of a galaxy allows for an estimate of its axis ratio, e, position angle, θ_e, and effective radius, R_e. It also allows us to trace the stellar components of a galaxy in order to estimate its stellar mass profile. This is done using the assumption that the luminous fraction within a given radius, R, is equal to the stellar mass fraction within the same radius, i.e.,

$$\frac{L(<R)}{L_{\rm tot}} = \frac{M_*(<R)}{M_*}. \tag{2.2}$$

A galaxy can be thought of as consisting of two components, a central bulge and an extended disc. The central bulge is well described by a de Vaucouleurs profile[14], $R^{1/4}$ profile, whereas Sérsic found that the extended disc profile is better described by an exponential profile[54]. Sérsic, observing that different galaxies are a mixture of bulge and disc components, generalised the de Vaucouleurs profile and developed the so-called Sérsic profile[54], also known as Sérsic's $R^{1/n}$ model. This states that the surface brightness, I, depends on the radius, R, as follows

$$I(R) = I_e \exp\left\{-b_n\left[\left(\frac{R}{R_e}\right)^{1/n} - 1\right]\right\} \tag{2.3}$$

where I_e is the surface brightness at the effective radius, b_n is a constant dependent on the index n and R_e is the effective radius defined as the radius within which half of the total light from the model can be found,

$$\int_0^{R_e} I(R)R\mathrm{d}R = \frac{1}{2}\int_0^{\infty} I(R)R\mathrm{d}R. \tag{2.4}$$

Since our observations are on the celestial sphere and projected along our line of sight, we can integrate Eq. (2.3) over a projected area to get an expression for the cumulative luminosity of the system within a circle of radius R,

$$L(<R) = \int_0^R I(R')2\pi R'\mathrm{d}R' \tag{2.5}$$

and arrive at a final equation for the total luminosity,

$$L_{\rm tot} = 2\pi E_e e^{b_n}\frac{n(2n-1)!R_e^2}{(b_n)^{2n}}. \tag{2.6}$$

For a derivation of this equation, see Appx A.1. Ciotti (1991)[12] found an approximation of $b_n = 2n - 0.342$ for $0.5 \leq m \leq 10$ with relative errors less than 0.001. From this, the de Vaucouleurs profile would have $b_4 = 7.676$ and for the exponential profile $b_1 = 1.676$. Figure 2.3.1 shows the Sérsic profile for different values of n. Larger n values have a steeper luminosity profile in the inner region and extended wings in the outer region, whereas lower n values have a much shallower profile in the inner region and a steep truncation further out.

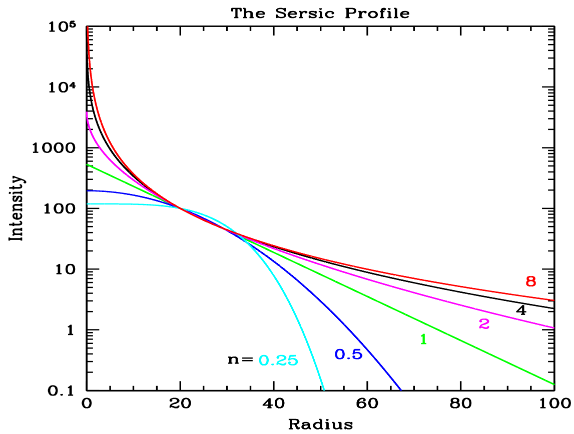

Figure 2.3.1: Sérsic profiles for varying values of n. The $n = 4$ model represents the de Vaucouleurs profile, $n = 1$ models represents an exponential model. The range of models covered by the Sérsic profile is the reason for its wide use. This image was obtained from the GALFIT manual[44].

The profile which has been most successful at reproducing observations of elliptical galaxies is the de Vaucouleurs profile. In this case, Eq.(2.3) would give a relation between luminosity, effective surface brightness and effective radius of

$$L_{\text{tot}} \approx 7.21\pi I_e R_e^2. \tag{2.7}$$

2.3.2 Scaling laws and the Fundamental Plane, FP

Many of the physical properties of elliptical galaxies are correlated. Understanding these correlations not only help with putting constraints on our theoretical models but also allow us to infer measurements as a result of these relations. For example, we can estimate an elliptical galaxy's distance by measuring its central velocity dispersion and using a relationship between velocity dispersion and luminosity for galaxies at known distances. Using parameter correlation techniques it has also been possible to show that dwarf elliptical galaxies are fundamentally different to elliptical galaxies, shown in their low surface brightness[60], one such example is M32.

From the virial theorem we see that the mass, M, of a galaxy is fundamentally

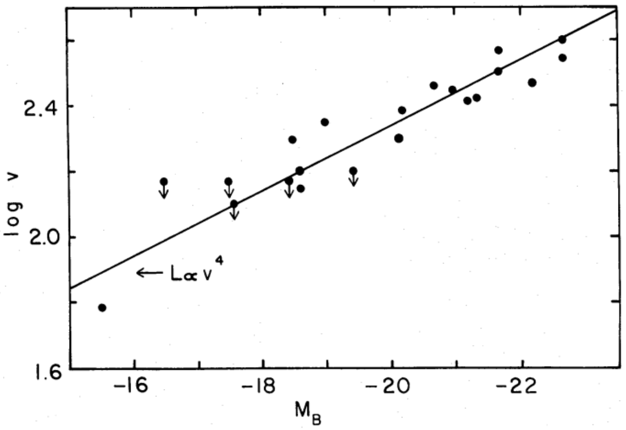

Figure 2.3.2: Line of sight velocity dispersion plotted against absolute magnitude. The point with the smallest velocity corresponds to M32. This demonstrates that the galaxies studied are consistent with the relation $L \propto \sigma_v^4$. The image was obtained from Faber & Jackson 1976[21]

related to its velocity dispersion, σ_v, through the relation

$$\frac{M}{R} \propto \sigma_v^2. \tag{2.8}$$

Eq. (2.6) shows that $L \propto I_e R^2$ and so assuming a constant surface brightness and a constant mass-to-light ratio we can arrive at the special case for the Faber-Jackson relation of

$$L \propto \sigma^4 \tag{2.9}$$

where the Faber-Jackson relation[21] states that $L \propto \sigma^\gamma$.

The $\gamma = 4$ model matches observations of elliptical galaxies well as shown in Fig. 2.3.2. This assumption has been studied further and a more accurate representation of the observations would be $L \propto \sigma^{3.1}$ for less massive galaxies and $L \propto \sigma^{15.0}$ for more massive galaxies[30]. The difference is thought to arise from the different formation mechanisms, where more massive galaxies are formed through merging, as discussed previously, and less massive galaxies are formed through dissipation.

The Fundamental Plane

The parameter correlation that elliptical galaxies show can be characterised by the FP. Starting with the virial theorem, and stating that for elliptical galaxies the gravitational potential energy is given by $U = -GmM/r$ and the kinetic energy is given by $T = m\sigma_v^2$, we can derive a relation between surface brightness, I, radius, R, and the velocity dispersion, σ_v

$$\sigma_v^2 = \pi G R L \Upsilon \tag{2.10}$$

where Υ is the mass-to-light ratio. When considering a constant Υ it should be noted that this is only an approximation valid in the inner region of a galaxy, defined by $R_e/8$, and so the velocity dispersion discussed is the velocity dispersion within the inner region, $\sigma_v = \sigma_0$. Eq. (2.10) is often written in the form $\log R_e = \log L - 2\log\sigma_0 + \gamma$, where γ is some constant. The average surface brightness, $\langle SB\rangle_e$ is related to L through, $\langle SB\rangle_e = 42.05 - 2.5\log(L/2\pi R_e^2)$ leading to a

$$\log R_e = 2\log\sigma_0 + \frac{1}{2.5}\langle SB\rangle_e + \gamma. \tag{2.11}$$

In reality, the observed fundamental plane is tilted with respects to the derived FP and so the constants before each term in Eq. (2.11) are better represented by a more general form

$$\log R_e = \alpha\log\sigma_0 + \beta\langle SB\rangle_e + \gamma \tag{2.12}$$

where α, β and γ are some constants which are dependent on the filter that is used for an observation. It is these three parameters, $\log R_e$, $\log\sigma_0$ and $\langle SB\rangle_e$ which are used to define the FP. Projections of the FP can be seen in Fig. 2.3.3 which were obtained from Kormendy & Djorgovski (1989)[38].

Values for α β and γ have been estimated over the years. In 1987, Djorgovski and Davis found the values of $\alpha = 1.49$ and $\beta = 0.90$, but used a modified radius defined as $R_e = a_e/\sqrt{1-\epsilon}$. In the same year, Dressler et al. found in the Johnson B passband that $\alpha = 1.325$ and $\beta = 0.825$.

The power of the FP can be seen in the following example relation derived by Dressler et al. (1987)[16]. Suppose a diameter, D_n, defined as the diameter within which $I_e = 20.75\,\mathrm{mag\ arcsec^{-2}}$ in the B-band surface brightness. The de Vaucouleurs $R^{1/4}$ scaling law for the surface brightness suggests that D_n/R_e is larger for galaxies with a higher surface brightness. Therefore, $D_n \propto R_e I_e^{0.8}$ or

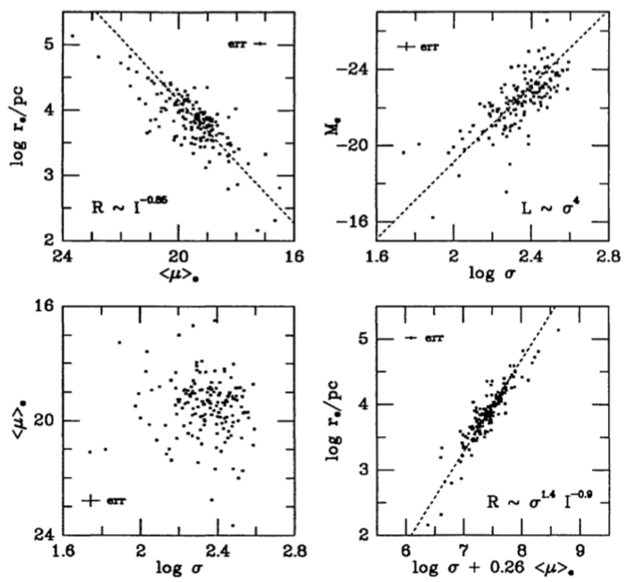

Figure 2.3.3: Projections of the FP showing the relation between: *top left*, effective radius R_e, here r_e, and the mean surface brightness $\langle SB \rangle_e$, here $\langle \mu \rangle_e$; *top right*, luminosity L_e in magnitudes, here M_e, and velocity dispersion σ_v which shows the Faber-Jackson scaling relation; *bottom left*, surface brightness and velocity dispersion, this can be thought of as the FP as seen face-on; *bottom right*, radius and a combination of surface brightness and velocity dispersion, this can be thought of as the FP seen edge-on.

$D_n \propto \sigma_0^{1.4} SB_e^{0.07}$. Using the Virgo cluster, Dressler et al. [15] derived

$$D_n = 2.05 \left(\frac{\sigma_0}{100\,\mathrm{km\ s^{-1}}} \right)^{1.33} \mathrm{kpc} \tag{2.13}$$

which has a scatter in D_n of about 15%. This scaling relation is known as the $D_n - \sigma_0$ correlation.

2.4 Dark Matter, DM

DM arose as a possible solution to the missing mass problem, first realised in 1937 when Fritz Zwicky estimated the radial velocities as a function of distance from the galaxy centre, or rotation curves, for galaxies in the Coma cluster[64]. His conclusion at the time was that the galaxies within the Coma cluster had a much higher mass-to-light ratio than other local galaxies, by a factor of about 200. Either this was true and the stars within the galaxies of the Coma cluster were fundamentally different to those of the Milky Way, or there was an additional, unobserved, mass component present. An example of the rotation curves observed for NGC 3198 is shown in Fig. 2.4.1.

As to the physical nature of DM, much is still unknown. The only property

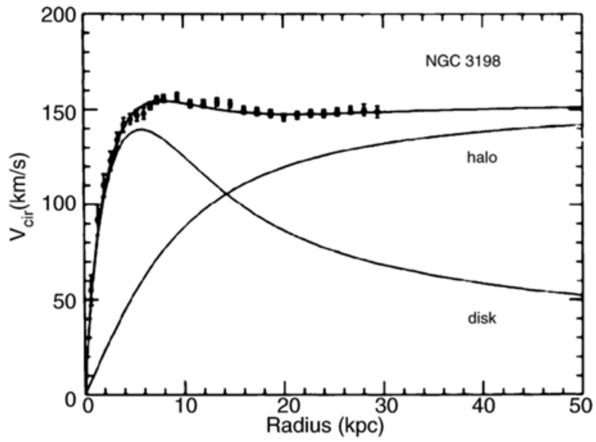

Figure 2.4.1: An example of the expected rotation curve (labelled disk) compared to the actual rotation curve of NGC 3198 and the inferred dark matter component (labelled halo). Figure obtained from Schneider (2006)[51]

that will be assumed true in this thesis is that DM only interacts with baryonic matter and light through their gravitational fields.

An estimation of DM's distribution within a galaxy can be done by balancing the gravitational force of a galaxy with its centrifugal acceleration, to arrive at the Kepler rotation law,

$$v^2(R) = \frac{GM(< R)}{R}. \tag{2.14}$$

From this we can make an estimation of the luminous mass profile by assuming a constant Υ in the inner, baryonically dominated, region. Therefore, an estimation of the luminous mass profile would give us the mass profile and thus an estimation of the rotation curve that would be expected, were there only luminous mass present

$$v_{\mathrm{lum}}^2 = \frac{GM_{\mathrm{lum}}(< R)}{R}. \tag{2.15}$$

The difference between these profiles can be termed the DM rotation curve, given by,

$$v_{\mathrm{DM}}^2 = v^2 - v_{\mathrm{lum}}^2 \tag{2.16}$$

$$\therefore M_{\mathrm{DM}}(< R) = \frac{R}{G}\left[v^2(R) - v_{\mathrm{lum}}^2(R)\right]. \tag{2.17}$$

As can be seen from Fig. 2.4.1, the shape of the rotation curve implies that

DM dominates the total mass budget at large radii. This is the origin of the DM halo model. Due to the lack of kinematic tracers in elliptical galaxies at large radii it is difficult to quantify the extent to which these DM halos extend. A lower limit can be set by looking at the 21-cm hydrogen line but these tracers are lacking further out where the orbits of satellite galaxies have been used to extend the lower limit even further. The results suggest that depending on how the baryonic matter is distributed, the DM distribution is such so that the overall matter profile of $\rho \propto r^{-2}$. This observed phenomenon of a finely tuned total mass distributions is known as the *dark matter conspiracy*.

Chapter 3

Estimating the luminous mass of elliptical galaxies

This chapter will describe the process of modelling the luminosity profile and the Spectral Energy Distribution, SED, of galaxies. Combining the two methods will allow us to estimate the stellar mass profile of galaxies. We will show how the method works, focussing in particular on a strong lensing system which is comprised of 2 lenses, G1 and G2, and 4 multiple images, A, B, C and D, of a single source. The lenses are members of the galaxy cluster MACS1115.9+0129, shown in Fig. 3.0.1 and the lensing system, which is located in the white box at the top of the cluster image, is enlarged in Fig. 3.0.2. At the end of the chapter, the redshift values of G1, G2 and the source will be estimated by looking at the available spectroscopic data.

3.1 The system

G1 is a spectroscopically confirmed member, see Sect. 3.5 of one of the *CLASH*[46] galaxy clusters. G1 is the main lens that produces 4 multiple images of a background source. The cluster is found at R.A.$_{\mathrm{J2000}}$ = 11:15:52.05 and Dec.$_{\mathrm{J2000}}$ = +01:29:56.6 and is measured to be at redshift $z = 0.352$[46]. G1 is $\sim 120''$(600 kpc) away from the cluster centre, assumed here to be located at the luminosity centre of the brightest cluster galaxy. At the cluster redshift, $1''$ corresponds to 4.97 kpc in the standardΛ CDM model, with$\Omega_m = 0.3$,$\Omega_\Lambda = 0.7$ and $H_0 = 70\mathrm{kms}^{-1}\mathrm{Mpc}^{-1}$, which is in close agreement with the measured values[24]. There are four multiple

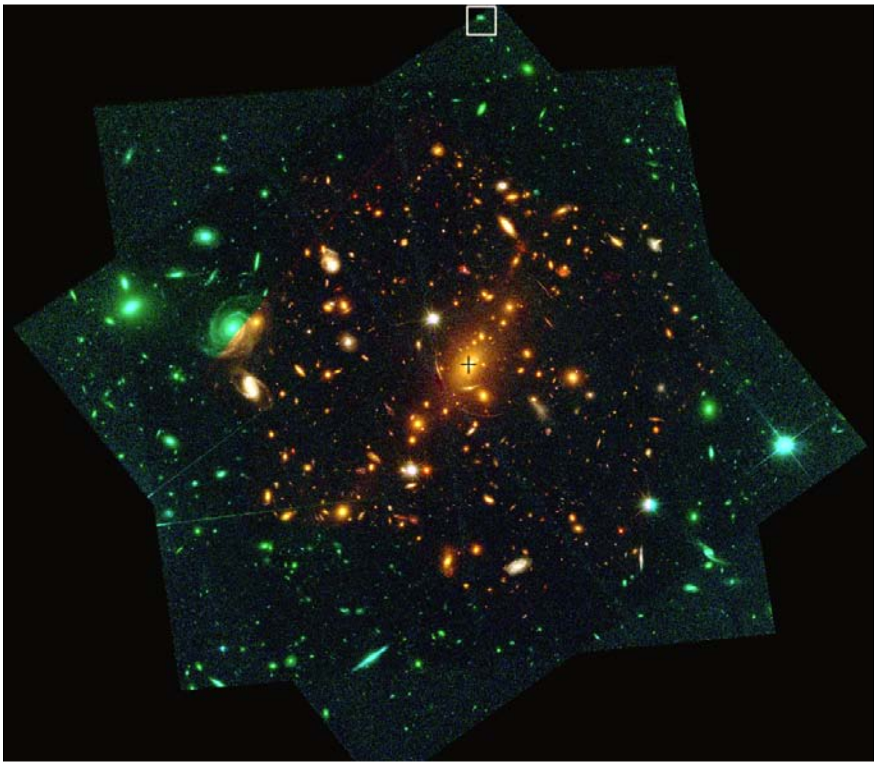

Figure 3.0.1: Colour image of the cluster MACS1115.9+0129 composed of all available *HST* broadband filters. The system studied in this project is shown in the white square at the top of the image, located 120″ away from the centre of the brightest cluster galaxy, marked by the black cross in the middle of the image.

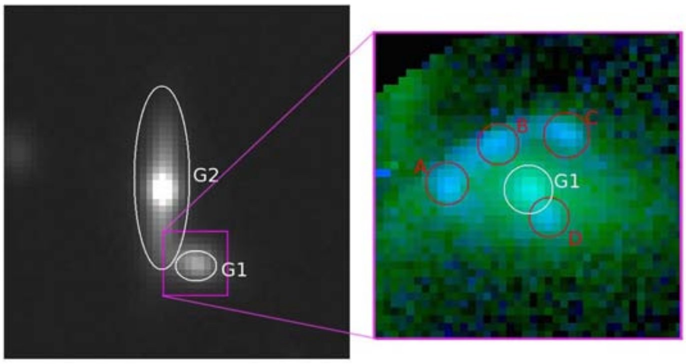

Figure 3.0.2: The system being studied, observed by Subaru (left) and *HST/ACS* (right). The higher resolution of *HST/ACS* allows the images of the distant source to be viewed separately from G1.

images surrounding G1, all coming from the same, more distant source, evident from the similarity in colour. G2, which is a nearby galaxy, also affects the positions of the multiple images, as well as their shapes.

3.2 The data

The data used to analyse the system was collected using both the ground-based Subaru telescope as well as the Hubble Space Telescope, *HST*, Advanced Camera for Surveys, *ACS*. Due to the fact that Hubble is in orbit, the observations are not limited by atmospheric influences and can reach a higher resolution than those obtained by Subaru, $\sim 1''$. The pixel scale of the *HST/ACS* and Subaru observations are $0.065''$ and $0.2''$, respectively. The Subaru observations were used to study G2, since the galaxy was out of the field of view of the *HST/ACS* observations.

3.2.1 The Cluster Lensing And Supernova survey with Hubble, *CLASH*

CLASH is a programme which observed 25 galaxy clusters between November 2010 and July 2013, totalling 524 orbits of time on the *HST*. The 524 orbits were divided into 474 orbits for cluster imaging and simultaneous supernova search, with the remaining 50 orbits reserved for follow-up supernova observations. The main science goals of the *CLASH* programme are:

- Map the distribution of DM is galaxy clusters using strong and weak gravitational lensing.
- Study the internal structure and evolution of the galaxies in these clusters, as well as the lensed, more distant source galaxies.
- Detect some of the most distant galaxies out to $z > 7$.
- Detect type Ia supernova out to redshift $z \sim 2$ to measure the cosmological parameters.

The cluster observations were carried out in 16 passbands using *WFC3/UVIS*, *WFC3/IR* and *ACS/WFC*. Table 3.1 shows an overview of the 25 galaxy clusters observed by *CLASH*, with the cluster of this thesis highlighted. The cluster sample was selected based on: 1) a circularly symmetric X-ray surface brightness distribution, an indication of a dynamically relaxed cluster; 2) an X-ray gas temperature > 5 keV, a characteristic of massive clusters; 3) a large enough sample to measure the mean mass concentration to 10% accuracy.

A follow up programme started in October 2010 and is still ongoing as part of the *ESO* Large Programme using the VIsible MultiObject Spectrograph, *VIMOS*, instrument of the European Southern Observatory's, *ESO*, Very Large Telescope, *VLT*. The immediate goals of the *CLASH/VLT* programme is to obtain redshift measurements of

Table 3.1: The *CLASH* Cluster Sample and *HST* Observation Plan from Postman et al. 2012[46]. The galaxies studied in this thesis reside in the cluster MACS1115.9+0129, highlighted in the table below.

Cluster	α_{J2000}	δ_{J2000}	z_{Clus}	HST Cycle	CLASH Orbits	Program ID	Archival Orbits[c]
X-ray Selected Clusters:							
Abell 209	01:31:52.57	−13:36:38.8	0.206	19	20	12451	(3)
Abell 383	02:48:03.36	−03:31:44.7	0.187	18	20	12065	(3)
MACS0329.7−0211	03:29:41.68	−02:11:47.7	0.450	19	20	12452	(2.5)
MACS0429.6−0253	04:29:36.10	−02:53:08.0	0.399	20	20	12788	(0.5)
MACS0744.9+3927	07:44:52.80	+39:27:24.4	0.686	18	17	12067	6
Abell 611	08:00:56.83	+36:03:24.1	0.288	19	18	12460	2
MACS1115.9+0129	11:15:52.05	+01:29:56.6	0.352	19	20	12453	0.5
Abell 1423	11:57:17.26	+33:36:37.4	0.213	20	20	12787	(0.5)
MACS1206.2−0847	12:06:12.28	−08:48:02.4	0.440	18	20	12069	0.5 + (0.5)
CLJ1226.9+3332	12:26:58.37	+33:32:47.4	0.890	20	18	12791	16
MACS1311.0−0310	13:11:01.67	−03:10:39.5	0.494	20	20	12789	0
RXJ1347.5−1145	13:47:30.59	−11:45:10.1	0.451	18	15	12104	6 + (0.5)
MACS1423.8+2404	14:23:47.76	+24:04:40.5	0.545	20	17	12790	5
RXJ1532.9+3021	15:32:53.78	+30:20:58.7	0.345	19	20	12454	(0.5)
MACS1720.3+3536	17:20:16.95	+35:36:23.6	0.391	19	20	12455	(0.5)
Abell 2261	17:22:27.25	+32:07:58.6	0.224	18	20	12066	(0.5)
MACS1931.8−2635	19:31:49.66	−26:34:34.0	0.352	19	20	12456	0
RXJ2129.7+0005	21:29:39.94	+00:05:18.8	0.234	19	20	12457	(1)
MS2137−2353	21:40:15.18	−23:39:40.7	0.313	18	18	12102	5 + (7)
RXJ2248.7−4431 (Abell 1063S)	22:48:44.29	−44:31:48.4	0.348	19	20	12458	(0.5)
High Magnification Clusters:							
MACS0416.1−2403	04:16:09.39	−24:04:03.9	0.42[b]	19	20	12459	(1)
MACS0647.8+7015	06:47:50.03	+70:14:49.7	0.584	18	18	12101	9
MACS0717.5+3745	07:17:31.65	+37:45:18.5	0.548	18	17	12103	7
MACS1149.6+2223	11:49:35.86	+22:23:55.0	0.544	18	18	12068	5
MACS2129.4−0741	21:29:26.06[a]	−07:41:28.8[a]	0.570	18	18	12100	5

Notes.
[a] Central cluster coordinates derived from optical image instead of X-ray image.
[b] Cluster redshift for MACS0416.1−2403 is based on *Chandra* X-ray spectrum (this work). Uncertainty on this value is ±0.02. For this fit, the core was not excluded. To maximize the counts, an aperture of 714 kpc was used, binned to achieve a minimum of 20 counts per energy bin. The background in the 0.7-7.0 keV range was fitted from the *Chandra* deep fields.
[c] Archival *ACS* or *WFPC2* imaging data only; *WFPC2* orbits shown in parentheses. Archival *ACS* images, when available, are used in conjunction with new CLASH data to achieve the desired depths in all filters.

- 400-600 cluster galaxies found in the 14 southern galaxy clusters of the *CLASH* sample, over the entire cluster volume.
- 10-30 lensed multiple images in the core of each cluster.

The end goals of the programme is to combine the *CLASH/VLT* data with the previous *CLASH* data to accurately measure the DM mass profiles of the clusters and cluster members, as well as to measure the internal dynamics of the clusters.

For the data used in this thesis, *VIMOS* was used in the Multi-Object Spectroscopy, MOS, mode using the low resolution blue grism with a wavelength coverage of 3700-6700Å.

With data releases, *CLASH* also releases key data relating to any scientific paper accepted for publication, which includes wide-field Subaru data. There is a wealth of publications as a result of the *CLASH* programme, characterising the density profiles of massive galaxy clusters[42, 43], improving dark energy constraints with high redshift type Ia supernovae[50] and much more. A full list of publications can be found on the *CLASH* website[1].

It is of particular interest for this study the paper by Grillo et al.[28] where the authors investigated a strong lensing system which has a double source imaged five times by two ETGs. The configuration of the images allowed for the measurements of the velocity dispersions of the two lenses, which were found to be (97 ± 3) km s^{-1} and (240 ± 6) km s^{-1}. The DM fraction found within the effective radii of the lens galaxies are 0.51 ± 0.21 and 0.80 ± 0.32, respectively.

3.2.2 Subaru data

The Subaru observations were taken with the Subaru telescope at the National Astronomical Observatory of Japan in the B, V, R_C, I_C and z bands, see Fig. 3.2.1 and Table 3.2. The seeing during the observations, was $\sim 1''$ and therefore the multiple images of the lensed source are blended with that of the more luminous and extended G1.

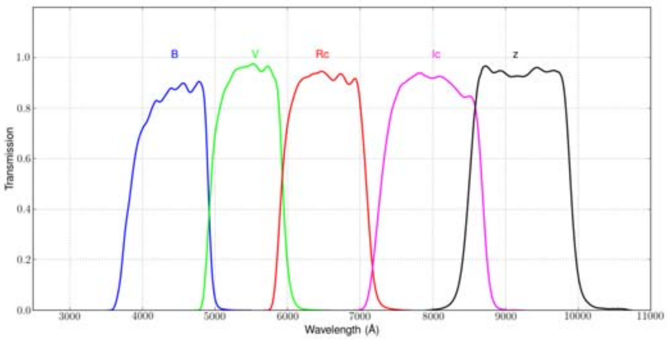

Figure 3.2.1: Transmission curves for the filters used in the Subaru data, obtained from the National Astronomical Observatory of Japan

G1 is an elliptical galaxy at redshift 0.352, whose red colour is characteristic of the typical old stellar population found in similar galaxies. As a result, we would expect that in the redder bands, I_C or z, the main contribution to the detected light would be from G1, while in the blue bands, especially in the B band, the source images would contribute more. All bands will be used while trying to model the luminosity profile of G1 and G2, but the varying contribution of the multiple

[1] http://www.stsci.edu/~postman/CLASH/Home.html

images of the source to the total luminosity profile will need to be considered when deciding upon the best model.

Table 3.2: A table of the Subaru data used in this thesis. The transmission curves for these filters can be seen in 3.2.1

FilterID	Exposure Time ($\times 10^3$ s)
B	2.40
V	2.16
R_C	2.88
I_C	2.16
z	3.96

3.2.3 *HST* data

The *HST/ACS* observations were taken by the *CLASH* team[46] where only 7 of the total 16 broadband filters had observations covering the system. The 7 bands used are listed in Table 3.3 and their respective transmission curves are shown in Fig. 3.2.2. The resolution of *HST/ACS* is sub-arcsecond and all but one of the multiple images are clearly resolved in these observations, see Fig. 3.0.2. Despite the unresolved image, D, being so close to G1 and their luminosity profiles' overlap, the centre of the image is still clear and this is not a hindrance when performing the strong lensing modelling. The overlapping luminosity profiles do cause some concern when modelling the luminous profile of G1, as discussed in Sect. 3.3.2.

Table 3.3: A table of the *HST* data used in this project. The transmission curves for these filters can be seen in 3.2.2

FilterID	Filter Central Wavelength (nm)	Filter Width (nm)	Exposure Time ($\times 10^3$ s)
f435w	429.7	103.8	3.828
f475w	476.0	145.8	3.728
f606w	590.7	234.2	3.870
f625w	631.8	144.2	3.728
f775w	776.4	152.8	3.900
f814w	833.3	251.1	7.998
f850lp	944.5	122.9	7.784

The *HST/ACS* data has two orientations or pointings. This is due to the use of two CCDs which have a separation between them. By rotating the instrument, only a small central region is not covered by the observations. G1 is only visible in one of the two orientations and when a combined image with all *HST/ACS* bands was created this was accounted for by the inclusion of a weighted pixel image,

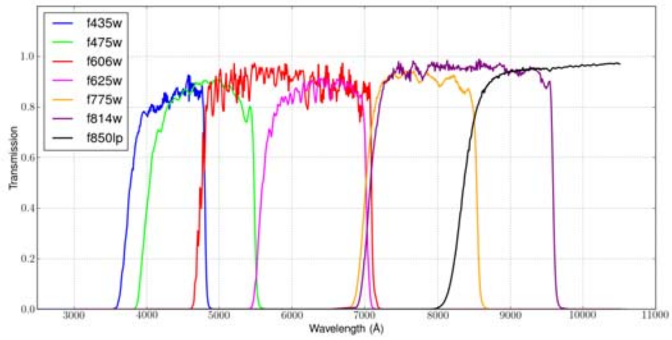

Figure 3.2.2: Transmission curves for the filters used in the *HST/ACS* data.

wht. The *wht* gives the relative "goodness" of an individual pixel, taking into consideration the exposure time, the pixel quality and saturation effects. Using the *wht* and knowing the exposure time of the science image, it is possible to estimate the uncertainty on each pixel.

3.2.4 Estimate of relative positions

The positions of the multiple images and the cluster centre are estimated relative to G1 using the *HST/ACS* data, averaging over all of the filters. Since G2 was out of the field of view of the *HST/ACS* data, the Subaru data was used for this galaxy. The results are shown in Table 3.4, where the errors on these values are the pixel size of the respective observations used. A useful value for comparing mass profiles obtained through luminosity modelling and lensing modelling, discussed in the next chapter, is an estimate of the Einstein radius, $\tilde{R}_{\mathrm{E}}$ which can be obtained by taking the average value of the multiple image distances from G1,

$$\tilde{R}_{\mathrm{E}} = \frac{1}{N_{\mathrm{I}}} \sum_{i}^{N_{\mathrm{I}}} D_i = 2.47\,\mathrm{kpc}. \tag{3.1}$$

where N_{I} is the number of multiple images, in our case $N_{\mathrm{I}} = 4$.

Table 3.4: The positions of G2 and of the multiple images, relative to G1. The position of the multiple images and that of the cluster centre were estimated using the *HST/ACS* observations, whereas Subaru Suprime observations were used for G2.

	G2	A	B	C	D	Cluster
x_1 ($''$)	-1.01	-0.708	-0.299	0.274	0.129	-4.22
x_2 ($''$)	2.30	0.008	0.399	0.469	-0.204	-121
Distance, D ($''$)	2.51	0.708	0.499	0.543	0.241	121
Distance, D (kpc)	12.57	3.52	2.48	2.70	1.20	601

3.3 Modelling the luminosity profile using GALFIT

We model here the galaxies' luminosity profiles from their photometry. In this way, when considering detailed lensing models, some constraints can be put on the values of the lens mass profiles. The main parameters that we would like to estimate are the values of ellipticity and position angle of both G1 and G2. This was done using the GALFIT[44] software developed by Chien Y. Peng.

GALFIT is an image analysis algorithm which models the light distribution of an object using analytic functions. It can be used to model an object as a whole or to model the individual components of a model, for example an extended object with a central bulge or two overlapping galaxies. GALFIT can only be used to fit functions and estimate the goodness of fit to an observation.

The model predicted pixel value at a given pixel, B_i, is compared to each pixel of the science image, $\mathrm{B}_i^{\mathrm{obs}}$ using the χ^2 method,

$$\chi^2 = \sum_{i}^{N_{\mathrm{B}}} \frac{(\mathrm{B}_i^{\mathrm{obs}} - \mathrm{B}_i)^2}{\sigma_i^2}, \tag{3.2}$$

where N_{B} is the number of pixels and σ_i is the error on that pixel. No attention is given to the χ^2 values obtained through modelling the luminosity profile as it is an estimation of the model fit, pixel by pixel. We are not trying to reproduce the whole image, we are only trying to find the parameters that best describes the ellipticity and orientation of the galaxies. A mask file is also supplied to minimise the effect of external light sources on the overall χ^2. The mask file indicates which pixels should be ignored when estimating the χ^2 of a model.

3.3.1 Software limitations

GALFIT does not extract Point Spread Functions, PSFs, nor mask neighbouring objects automatically. If these are required they must be done separately, before running GALFIT, and included in the input parameter file.

A PSF was created for each individual filter by using a star from a region close to the two galaxies, which was not saturated in the corresponding observation. The purpose of a PSF is to describe the response of an imaging apparatus to a point source. A point source is used because an extended object will add features

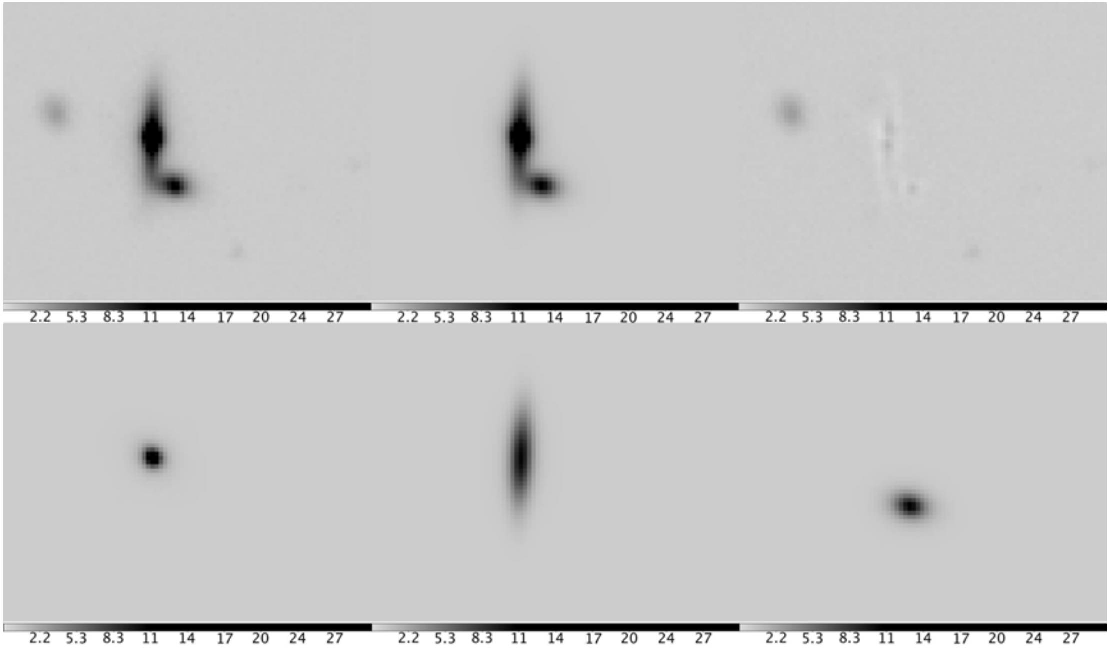

Figure 3.3.1: The results of the GALFIT modelling. *Top left*: the original observation in the Subaru z-band. *Top centre*: the reproduced image. *Top right*: the residual after subtracting the model from the observational data. *Bottom*: the three components of the model, G1, *left*, G2's bulge, *centre*, and G2's extended wings, *right*.

to the PSF which should not be confused as being features of the apparatus. A PSF which is elongated in a certain direction will allow the processing of the image to account for this by compressing the image in this direction. An image which has an ellipticity of 0.2 at a position angle of 0° would be considered elliptical, unless a PSF also exhibits the same ellipticity and position angle which would suggest that the object is in fact circular.

3.3.2 Modelling the luminosity profile

In all of the Subaru observations the multiple images are blended with that of G1, and therefore the light profile of G1 is contaminated by that of the lensed source. Any estimates of the luminosity profile for G1, obtained using Subaru data, is therefore not reliable. G2 is distant enough from the multiple images that their luminosity profiles are not blended significantly. For these reasons, in the following we will model the luminosity profile of G2 using the Subaru data and that of G1 using the *HST* data.

Firstly, G1 and G2 are modelled in the Subaru images as single components. Both are modelled using Sérsic profiles, Eq. (2.3), allowing the central positions of the galaxies, effective radius, R_e, the Sérsic index, n, the axis ratio, $e = 1 - q$, and the position angle, θ_q, to be optimised. No accurate model is obtained for

G2, most probably due to the fact that G2 seems to have a bulge component as well as an extended disc component. In order to account for this, an additional component is added to G2. The results are summarised in Table 3.5 and the model components are shown in Fig. 3.3.1. The residual image, shown on the top right of Fig. 3.3.1, shows that there is still some minor over-subtraction occurring. The relevant parameters for the lens modelling discussed in the next chapter, are e and θ_e. Looking at the subcomponents of G2, it is evident that the position angle is well represented by our model. Consistent results are found for the ellipticity of G2 when modelling is done in the different filters. Combining the results from all of the filters, the values for the position angle and ellipticity are estimated, where the error on these were chosen from the variance: $\theta_e = (-2 \pm 15)^\circ$ and $e = 0.2 \pm 0.15$.

Table 3.5: The optimised parameter values for the z-band. The residuals image obtained from the optimisation in the z-band was the best of all of the filters. The values for G1 have been included, but a more detailed modelling of its luminosity profile is done later on in this chapter using *HST/ACS* data.

Component	x_1 (arcsec)	x_2 (arcsec)	R_e (arcsec)	n	e	θ_e ($^\circ$)
G1	0	0	0.6	1.19	0.51	79.5
G2 bulge	-1.01	2.30	0.1	12.08	0.66	55.8
G2 disc	-1.01	2.30	1.6	0.54	0.15	-2.71

Table 3.6: The optimised parameter values for the composite image, as well as for the f850lp filter. The residual image obtained from the optimisation of the composite image was the best of all of the filters and is shown in Fig. 3.3.2.

Band	R_e (arcsec)	n	e	θ_e ($^\circ$)
total	0.65	3.29	0.66	73.5
f850lp	0.71	1.85	0.69	77.1

For G1, we use an image that is a combination of all of the available *HST/ACS* filters listed in Table 3.3. From the `GALFIT` modelling, the obtained parameters of G1 are $q_1 = 0.34$ and $\theta_{q_1} = 73.5^\circ$. Trying to get a consistent model with good residuals in the individual filter observations is difficult because of the close proximity of G1 and image D. It is for this reasons that the errors assumed on these values, when used later on in parametrising the lensing models, are taken to be conservative, $q_1 = 0.3 \pm 0.15$ and $\theta_{q_1} = (70 \pm 15)^\circ$. The original science image, the model and the residuals obtained from modelling are shown in Fig. 3.3.2.

From the reconstructed luminosity profile it was possible to estimate the fraction of light enclosed within increasing apertures. This will be converted in the

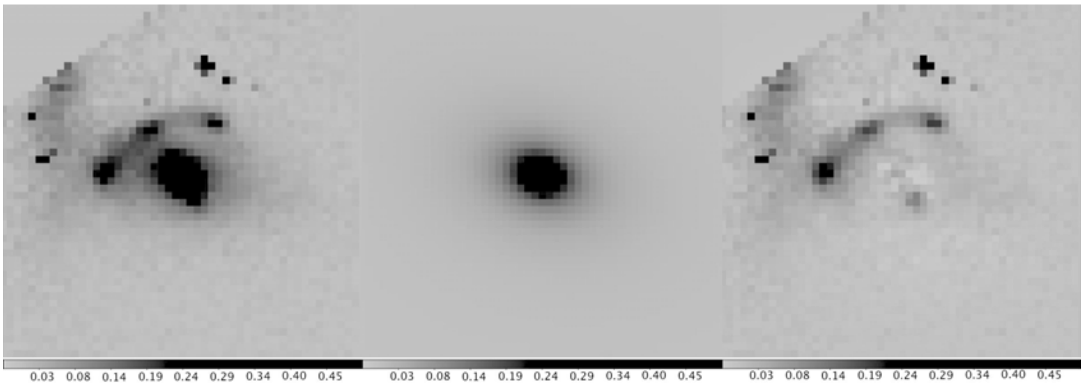

Figure 3.3.2: The original observation (left), the model (centre) and the residual (right) obtained from modelling the luminosity profile of G1. The original image is a composite image of the filters named in Table 3.3. From this, values of $q_1 = 0.3 \pm 0.15$ and $\theta_{q_1} = (70 \pm 15)^{\circ}$ were obtained.

following section into a luminous mass profile.

3.4 Fitting the Spectral Energy Distribution, SED

A galaxy emits light at a wide range of wavelengths. With the exception of galaxies which have a dominant contribution from an active galactic nucleus, a galaxy's spectrum is dominated by the light emitted from the stars within the galaxy. This light could come directly from the stars, or be absorbed by the interstellar medium and re-emitted at different wavelengths. The total luminous mass of a galaxy can be obtained by matching the observed magnitudes in the different bands with synthesised spectra, created from stellar templates and convolved with the different filter transmission curves. The creation of the synthesised spectra is known as *isochrone synthesis*[11], whereas the matching of these spectra to our filter magnitudes is known as Spectral Energy Distribution, SED, fitting.

The software used to perform SED fitting was `LePHARE`[1]. `LePHARE` is a set of Fortran commands employed to perform SED fitting and estimate photometric redshifts. Using Bruzual and Charlot[7] templates and fixing the redshift values to those found in the next section, we estimate the total luminous mass values of G1 and G2, starting from their observed magnitudes in different filters. Luminous masses obtained through SED fitting are typically accurate to $\sim 30\%$ depending on the adopted templates and modelling details.

SED fitting is dependent on the following parameters: the dust extinction, the metallicity, the Star Formation Rate, SFR, and the stellar Initial Mass Function, IMF. The dust extinction is used to account for any reddening that results from the absorption and re-emission of light by the dust in the Inter Stellar Medium, ISM. The dust extinction is accounted for by using the reddening function generated by Calzetti et al.[8]. The metallicity, SFR and stellar population age are modelled with Simple Stellar Populations, SSP, i.e. a single age, single abundance collection of stars whose luminosity distribution depends on the initial distribution and the assumed age. The age is incrementally increased in order to find the best fitting SSP.

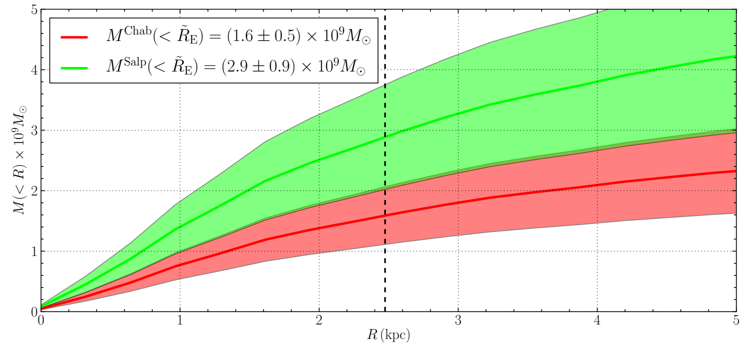

Figure 3.4.1: The luminous mass profile for G1 assuming a Chabrier IMF (red) and a Salpeter IMF (green). The black dotted line shows the location of $\tilde{R}_{\rm E}$ and the filled in area of the plot represent the 30% confidence intervals.

The main source of uncertainty is associated to the choice of the IMF, which describes the distribution of stellar masses that form in a star-formation event in a given volume. The two most commonly used stellar IMFs are the Salpeter[49] and Chabrier[10] IMFs, which effect the estimation of the total luminous mass by a factor of nearly 2, with $M_*^{\rm Salp} \approx 1.8 M_*^{\rm Chab}$. The best-fitting SED models provide estimates of the total luminous mass of G1 and G2 of $4.3 \times 10^9 M_\odot$ and $9.5 \times 10^{10} M_\odot$, using a Chabrier Initial Mass Function, IMF. This translates to a total luminous mass of $7.8 \times 10^9 M_\odot$ and $1.6 \times 10^{11} M_\odot$ for G1 and G2, respectively, using a Salpeter IMF. Combining these estimates with the luminosity profiles obtained earlier, a total luminous mass profile for G1 is obtained and is shown in Fig. 3.4.1. The stellar mass of G1 for both IMFs, at the Einstein radius, are $M^{\rm Chab}(<\tilde{R}_{\rm E}) = (1.6 \pm 0.5) \times 10^9 M_\odot$ and $M^{\rm Salp}(<\tilde{R}_{\rm E}) = (2.9 \pm 0.9) \times 10^9 M_\odot$.

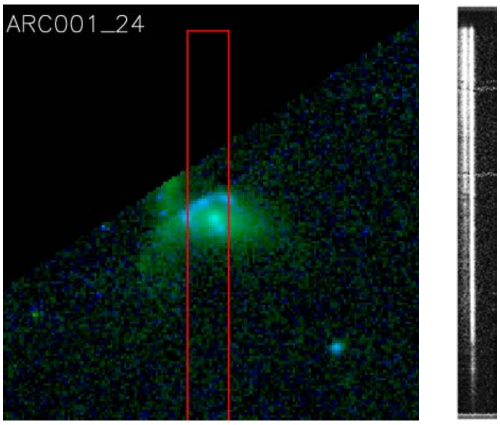

Figure 3.5.1: The slit position overlaid on the *HST/ACS* image (left) and the raw *VLT/VIMOS* spectra from the grating (right).

3.5 Estimating the redshifts of G1, G2 and the source

Spectroscopic data was obtained from *CLASH/VLT*. The observation had an exposure time of 1200 s, and the slit position is shown in Fig. 3.5.1, as well as the 2D spectrum. From the raw spectra shown, it is clear that there is more than one spectrum, the fainter one on the left corresponds to G2, while the brighter, more central spectrum is from G1. Due to the seeing and the slit orientation, the spectrum of G1 and that of the lensed source are merged into a single spectrum. This allows us to estimate the redshift values of both G1 and the source.

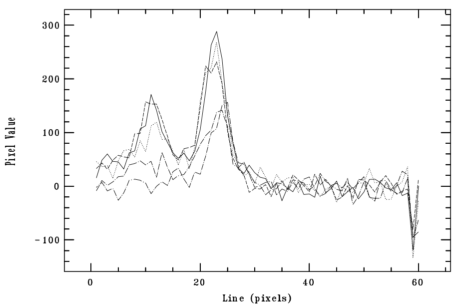

Figure 3.5.2: Slices of the spectrum taken at different wavelengths in order to check the alignment of the spectrum with the slit.

First, the alignment of the spectrum is checked. This is done by taking slices of the spectrum at varying wavelengths to see if there is a consistent peak position. Fig. 3.5.2 shows that the spectrum is well aligned and therefore no corrections need to be applied to straighten it.

Using the slit position of the peak flux value of Fig. 3.5.2 a suitable aperture is chosen to extract the spectrum, covering as much of the peak, while minimising the background contamination. With the extracted spectra, one could try and see if any spectral features are present. Since G1 and G2 appear as elliptical galaxies in the Subaru and *HST* images, we expect to see some typical absorption features.

The clearest identified feature is the K-H doublet found at rest-frame wavelengths of 3934.8Å and 3969.6Å. By aligning a template with this feature it is possible to estimate the redshift of G1 and G2, $z = 0.353$ and $z = 0.363$, respectively. The extracted spectra and the redshifted template features are shown in Fig. 3.5.3.

When the estimated redshifts are compared to the cluster redshift found by Postman et al.[46] of $z = 0.352$, these two lenses can be confirmed as being members of the cluster.

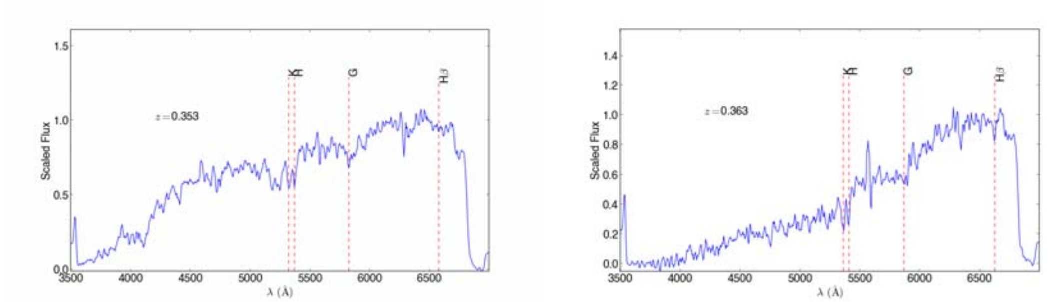

Figure 3.5.3: The spectrum of G1 (left) and G2 (right) with redshift-evolved template lines.

Comparing the two spectra, it is evident that there is an additional component in the spectrum of G1. This additional flux is likely to come from the lensed source. There is a clear break at $\lambda \sim 4200$ Å. Assuming that this is the Lyman-α break, the templates can be redshifted at the proposed values to see if other features are present. Fig. 3.5.4 shows such a plot and confirms that this is in fact the Lyman-α break for a source at redshift $z \sim 2.387$, with good alignment of the Si II and C IV lines. There is also a strong feature at 6301Å for the Al III line but since this is close to the sky emission line of O I found at 6300Å it is not clear whether this is an artefact of sky-subtraction or a true feature.

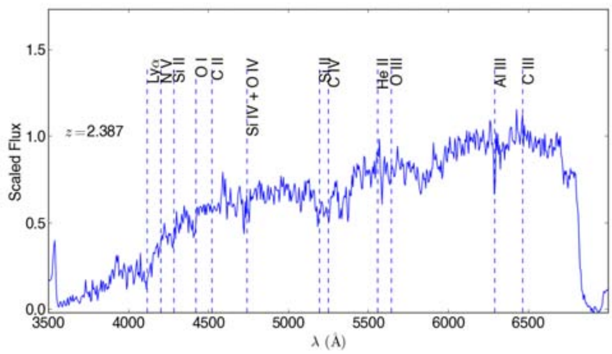

Figure 3.5.4: The spectrum of G1 with redshift-evolved template lines attempting to estimate the redshift of the lensed source.

Chapter 4

Total mass measurement of cluster members through strong lensing

This chapter will present how to estimate the projected total mass of galaxies using strong lensing models. The lensing system that we will consider is that presented in the previous chapter. This lensing system is of particular interest due to the possibility of it having a relatively low velocity dispersion as compared to previously studied lenses. We will look at increasingly complex models to reproduce at best the observed multiple image positions. From these models, we will be able to determine the projected total mass of the two lenses.

4.1 Lens models using `GRAVLENS`

The software used for modelling our lensing system was `GRAVLENS`[32, 33, 34], developed by Chuck Keeton. Specifically, this is a package, comprising of two individual stand-alone applications, `gravlens` and `lensmodel`. Capitalisation will be used to differentiate between the package and the applications, with lower case being used for the latter. When modelling a lens, `lensmodel` is used, whereas `gravlens` is used for basic lensing calculations. Details on the specific syntax of the software can be seen in the `GRAVLENS` manual[34].

The `alpha` model, available in the application, was used and is characterised by

$$\kappa = \frac{1}{2}(b')^{2-\alpha}\left[(s')^2 + \zeta^2\right]^{\alpha/2-1} \tag{4.1}$$

where κ is the convergence, see Sec. 1.2.1, b' is the lens strength, α is the power law index, related to the n value discussed in Sec. 1.3, s' is a central core radius at which the model flattens and ζ describes the elliptical radius in coordinates aligned with the major axis of the ellipse. ζ is defined as $\zeta = \left[(1-\epsilon)x^2 + (1+\epsilon)y^2\right]^{1/2}$ where ϵ is related to the axis ratio through $e^2 = (1-\epsilon)/(1+\epsilon)$. This model was used since it is possible to recover the expression for κ obtained in Sec. 1.3.1 for a SIS model by setting $\alpha = 1$ and $\epsilon = s' = 0$ in Eq. (4.1). In order to recover an SIE model, one would simple give non-zero values for ζ, characterised by the axis ratio, e, and a position angle, θ_e.

The parameters of the alpha model are p[1]: mass scale, (p[2], p[3]): galaxy position (x, y), p[4]: ellipticity defined as $q = (1-e)$, p[5]: position angle of the galaxy where p[5]=0 is defined as vertically along the y axis and positive values are anticlockwise from this position, p[8]: s' and p[10]: α.

4.1.1 Limitations of the software

`GRAVLENS` allows for the investigation of complicated models, but it has some limitations which need to be considered.

Eq. (1.29) states that the deflection angle and thus the mass is only dependent on the lens strength. In `GRAVLENS`, the lens parameters describing the mass are not independent from the ellipticity parameter, q. It is therefore difficult to scale the total masses of two components according to their measured luminosities. This issue is discussed further in a paper by Keeton[31].

In a situation where it is known that there are two mass components acting as lenses, it would be logical to assume a positive value for both of the lens strengths. It would also be logical to assert that one galaxy has a lens strength larger than another by observing that one is brighter and hence has a higher luminous mass. Neither of these features are available at the moment in `GRAVLENS`.

It should also be known that `GRAVLENS` uses a parametric mass model. Parametric models of a lens are easy to interpret physically. Non-parametric models do not have such a simple parameter space and as a result, might result in unphysical solutions, even if the observables are reproduced.

4.1.2 The models

Starting from a simple model with a small number of free parameters we will gradually increase the complexity of the model. At each step, we will see if the added complexity is justified by seeing how well the new model reproduces the multiple images and whether or not it is a plausible physical model.

The 2 lens models used are SIS and SIE, for each of the contributing masses, G1, G2 and the cluster. A SIS model is characterised by 3 parameters, x_1, x_2 and b, and an SIE by an additional 2 parameters, q and θ_q. The number of observables are 8, 2 for each image position coordinate ($\boldsymbol{x}_i$). In order to optimise the model, certain parameters are allowed to vary, these are known as free parameters. Every time a parameter is changed the χ^2 function is estimated on the multiple image positions,

$$\chi^2_{\rm pos} = \sum_{i}^{N_{\rm I}} \frac{||\boldsymbol{x}_i^{\rm obs} - \boldsymbol{x}_i||^2}{\sigma_{\boldsymbol{x}}^2}, \tag{4.2}$$

where $N_{\rm I}$ is the number of multiple images, and for the i-th image, $\boldsymbol{x}_i^{\rm obs}$ is the observed position vector, $\boldsymbol{x}_i$ is the model predicted position vector and $\sigma_{\boldsymbol{x}}$ is the error on the observed position vector. When limits are placed on the parameters an additional penalty is imposed on the χ^2 value, according to

$$\chi^2_{\rm plim} = \frac{(p - \tilde{p})^2}{\sigma_p^2} \tag{4.3}$$

where p is the tried parameter value, $\tilde{p}$ is the prior on the value of the parameter, and σ_p is the 1σ error of this parameter.

For the purpose of finding the best model, we compare the total χ^2 values between models, $\chi^2_{\rm tot} = \chi^2_{\rm pos} + \chi^2_{\rm plim}$. The number of degrees of freedom, $N_{\rm dof}$, is equal to the number of observables minus the number of free parameters. We will always quote the χ^2 value and the $N_{\rm dof}$. If a significant reduction in the $\chi^2_{\rm tot}$ is seen when adding a free parameter then it is reasonable to assume that the model better represents the system, as long as it is physically plausible. The observations are the positions of the multiple images, two coordinate values for each image. Therefore the mass profile is most accurately estimated at these positions, represented by a circle of radius $\tilde{R}_{\mathrm{E}}$, see Eq. (3.1).

BootStrapping analysis[17], BS, was done using the Monte Carlo method of generating 1000 synthetic data sets based on the observed positions of the multiple images. The synthetic data was created by generating 2 random numbers to represent the position of each of the multiple images, $(x_1, x_2)_i$. The random numbers were generated according to a Gaussian distribution centred on the observed position of the multiple images, $(x_1^{\mathrm{obs}}, x_2^{\mathrm{obs}})_i$, with a width equal to the pixel size of $0.065''$. The synthetic data sets were then used to re-optimise the already obtained best model parameters using `lensmodel`.

In the following presentation of the results, the headings of the different models are arranged as follows: the first model in the title refers to G1, the second to G2 and if there is a third one, this refers to the model used to represent the contribution from the cluster component. The quoted errors in this section are the 68% (1σ) confidence limits, unless stated otherwise, and all of the mass profiles shown have their origin, $R = 0$, at the luminous centre of G1. Only the $\alpha = 1$ power law model is considered in the following analysis, due to the low number of observables and the complexity of the system.

SIS + SIS

The starting point for modelling the mass profiles of the lenses is with a SIS profile. Since our system consists of 2 galaxies, G1 and G2, both galaxies contribute to the total mass at $\tilde{R}_{\mathrm{E}}$, and need to be included in the initial model. The only free parameters we have here are the position of the source, $\boldsymbol{y}$, and the strengths of G1 and G2, b_1 and b_2, respectively.

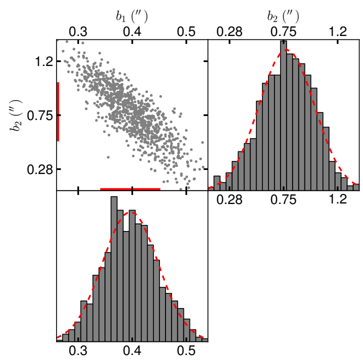

Figure 4.1.1: The free parameters where two SISs were modelled. The solid red lines indicate the 1σ (68%) confidence intervals, while the tick-marks have been placed at the 2σ (95%) confidence intervals, with the middle value simply being the midpoint of the 2σ values. The dotted red line is the best fitting function for the histogram using a Gaussian distribution.

The minimum χ^2 of this model is $\chi^2(N_{\mathrm{dof}}) = 8.43(4)$. The parameter val-

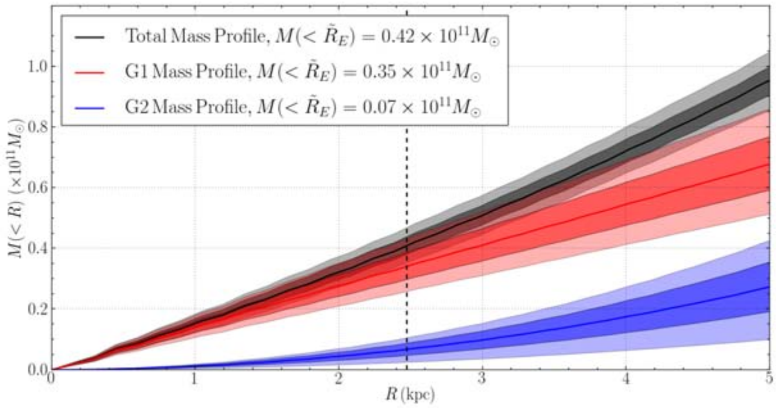

Figure 4.1.2: The total mass profile obtained through the bootstrapping analysis of a 2SIS model. The filled in areas represent the 1σ (68%) and the 2σ (95%) confidence intervals. $R = 0$ is defined as the centre of G1. $\tilde{R}_\mathrm{E}$ is the average of the multiple image distances from the lens centre, used as a consistent approximation of the Einstein radius for all models, and is represented here by the dotted line.

ues obtained from the optimisation, omitting the source position, are $b_1 = 0.35''$ and $b_2 = 0.99''$. From the BS analysis, the values and their respective statistical errors are $b_1 = (0.39 \pm 0.05)''$ and $b_2 = (0.78 \pm 0.2)''$. The resulting total combined mass profile, as well as the total mass profile for G1 and G2 individually, are shown in Fig. 4.1.2. At $\tilde{R}_\mathrm{E}$, $M_\mathrm{G1}(<\tilde{R}_\mathrm{E}) = (3.5 \pm 0.5) \times 10^{10} M_\odot$ and $M_\mathrm{G2}(<\tilde{R}_\mathrm{E}) = (0.7 \pm 0.2) \times 10^{10} M_\odot$ which are 83% and 17% of the total mass budget, respectively.

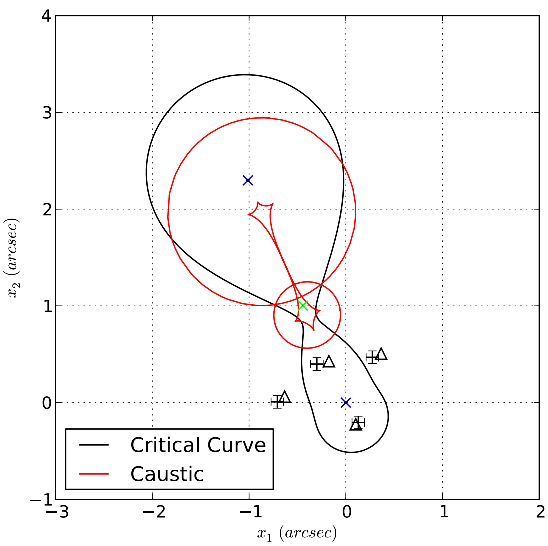

Figure 4.1.3: The critical curves (black curve) and the caustics (red curve) as seen on the lens plane and source plane respectively. The centre point of G1 and G2 are represented by a blue cross, with G1 found at $\boldsymbol{x}(0, 0)$ and the green cross represents the model predicted source position. The black '+' markers show the observable image positions with their errors of $0.065''$ and the '△' markers show the model predicted image positions.

In order to see whether or not the parameters were degenerate they were compared, as shown in Fig. 4.1.1. There is a clear degeneracy between the two parameters. This can be understood by considering the configuration of the model. We are trying to measure the projected total mass within the Einstein radius, where both galaxies contribute. A reduction in the contribution from G1 could be compensated for by an increase in the contribution from G2, and vice versa. The model predicted critical curves and caustics for the best 2SIS model are shown in Fig. 4.1.3

SIE+SIS

From the modelling of the galaxy luminosity profiles, discussed in the previous chapter, we have found that both galaxies have a certain degree of ellipticity. A logical next step would be to explore SIE models. We start by modelling G1 with a SIE profile because this is the main lens, and continue to approximate G2 with a simple SIS profile.

Table 4.1: The optimisation (opt) and the bootstrapping (BS) results from modelling G1 as an SIE and G2 as an SIS. The best model is the (SIE + SIS)$_2$ where θ_{q_1} is most stable.

		(SIE+SIS)$_1$			(SIE+SIS)$_2$			(SIE+SIS)$_3$		
			Free	Limits		Free	Limits		Free	Limits
$b_1('')$	opt	0.44	✓	-	0.43	✓	-	0.46	✓	-
	BS	$0.50^{+0.27}_{-0.07}$			$0.44^{+0.05}_{-0.05}$			$0.48^{+0.07}_{-0.05}$		
q_1	opt	0.30	✓	-	0.33	✓	0.4 ± 0.15	0.32	✓	-
	BS	$0.42^{+0.25}_{-0.16}$			$0.31^{+0.08}_{-0.09}$			$0.33^{+0.16}_{-0.13}$		
$\theta_{q_1}(^\circ)$	opt	58.9	✓	-	69.8	✓	70.0 ± 15	52.4	✓	-
	BS	65^{+30}_{-32}			$70^{+4.1}_{-3.5}$			56^{+28}_{-17}		
$b_2('')$	opt	0.89	✓	-	1.00	✓	-	0.82	✓	0.8 ± 0.3
	BS	$0.85^{+0.38}_{-0.50}$			$0.97^{+0.17}_{-0.18}$			$0.81^{+0.14}_{-0.10}$		
$\chi^2_{\rm pos}$		2.74			2.90			2.76		
$\chi^2_{\rm plim}$		0.00			0.22			0.01		
$\chi^2_{\rm tot}(N_{\rm dof})$		**2.74 (2)**			**3.12(2)**			**2.77(2)**		

Three different scenarios are explored, all of which have the same free parameters, b_1, q_1, θ_{q_1} and b_2. The first scenario has no parameter constraints, the second set the constraints of $q_1 = 0.4 \pm 0.15$ and $\theta_{q_1} = (70 \pm 15)^\circ$ using the values obtained from modelling the luminosity profile of the galaxies, the third only constrains b_2 with a conservative 1σ value and a starting value matching the previous results of the 2SIS model, $b_2 = (0.8 \pm 0.3)$ arcseconds. The most physically plausible model out of the three is model 2, as many of the Monte Carlo simulations in the other scenarios have improbable values for q_1 and θ_{q_1}. In both the first and third model, the 1σ values for θ_{q_1} are very high, resulting in many of the BS simulations having orientations which are not aligned well with the luminosity profile estimated earlier. The first model has an even bigger problem when looking at b_2, where the 68% confidence interval shows an error of about 80% and the lower 95% confidence interval tends to 0. For model 2, the χ^2 penalty for the imposed parameter constraints, $\chi^2_{\rm plim} = 0.22$, is small enough to keep the model's validity giving a final $\chi^2(N_{\rm dof}) = 3.12(2)$. This is a significant improvement on the 2SISs model and therefore the added complexity is justified. The results are shown in Table 4.1. In the second model, $M_{\rm G1}(< \tilde{R}_{\rm E}) = (4.0 \pm 0.5) \times 10^{10} M_{\odot}$ and $M_{\rm G2}(< \tilde{R}_{\rm E}) = (0.9 \pm 0.2) \times 10^{10} M_{\odot}$

SIE + SIE

As stated previously, both G1 and G2 are better represented by axially symmetric mass profile, rather than circular ones. It is for this reason that a model where both galaxies are SIEs is considered. To begin with, the model is optimised by varying the values of b_1, b_2, q_1 and θ_{q_1}, with q_2 and θ_{q_2} fixed to the values obtained from the luminosity modelling, see Section 3.3.2, $q_2 = 0.8$ and $\theta_{q_2} = -2.0°$. In a second run, parameter constraints are placed on q_1 and θ_{q_1}. In a third run, the values of q_2 and θ_{q_2} are allowed to vary with no parameter limits, and in a fourth and final run, constraints are place on q_1, θ_{q_1}, q_2 and θ_{q_2}. All of the parameter constraints are obtained from the luminosity modelling estimates. A summary of the χ^2 values for each model is shown in Tab 4.2.

The best model, where $\chi^2(N_{\rm dof}) = 0.53(2)$, is obtained when no parameter limits are imposed, and the free parameters are b_1, q_1, θ_{q_1}, and b_2. Despite this model's ability to reproduce the multiple image positions very well, the bootstrapping analysis shows that it is a rather unphysical model. For some of the parameter configurations, $b_2 \to 0$, meaning that a significant number of models have the total mass of G2 as zero. One of the limitations of the `lensmodel` software is the inability to assert that b_2 should remain larger than b_1, as is evident from their luminosity profiles, and therefore models with parameter limits have to be considered. This behaviour of b_2 is also observed in model 3, where constraints were only placed on q_2 and θ_{q_2} which leads one to suspect that b_2, q_1 and θ_{q_1} are degenerate. Both model 1 and 3 had very large 1σ values for θ_{q_1} allowing for orientations which did not match those found from modelling the luminosity profile. The models where

Table 4.2: The optimisation (opt) and the bootstrapping (BS) results for the models where 2 SIEs are considered.

		$2SIE_1$	Free	Limits	$2SIE_2$	Free	Limits	$2SIE_3$	Free	Limits	$2SIE_4$	Free	Limits
$b_1('')$	opt	0.41	✓	-	0.41	✓	-	0.41	✓	-	0.41	✓	-
	BS	$0.44^{+0.12}_{-0.07}$			$0.42^{+0.05}_{-0.05}$			$0.46^{+0.14}_{-0.07}$			$0.41^{+0.04}_{-0.05}$		
q_1	opt	0.19	✓	-	0.25	✓	0.4±0.15	0.21	✓	-	0.26	✓	0.4±0.15
	BS	$0.29^{+0.20}_{-0.13}$			$0.24^{+0.09}_{-0.09}$			$0.30^{+0.23}_{-0.14}$			$0.24^{+0.07}_{-0.09}$		
$\theta_{q_1}(^\circ)$	opt	50.7	✓	-	64.2	✓	70.0±15	46.8	✓	-	66.9	✓	70.0±15
	BS	59.6^{+49}_{-26}			$66^{+6.4}_{-7.8}$			53^{+55}_{-23}			$68^{+4.4}_{-4.9}$		
$b_2('')$	opt	1.93	✓	-	2.04	✓	-	1.92	✓	-	2.04	✓	-
	BS	$1.95^{+0.43}_{-0.59}$			$1.95^{+0.30}_{-0.30}$			$1.93^{+0.46}_{-0.71}$			$2.07^{+0.20}_{-0.28}$		
q_2	opt	0.80	×	-	0.80	×	-	0.81	✓	0.8±0.15	0.76	✓	0.8±0.15
	BS							$0.81^{+0.04}_{-0.03}$			$0.77^{+0.04}_{-0.03}$		
$\theta_{q_2}(^\circ)$	opt	-2.0	×	-	-2.0	×	-	-1.05	✓	-2.0 ± 15	-5.37	✓	-2.0 ± 15
	BS							$-1.72^{+3.7}_{-3.8}$			$-5.8^{+4.6}_{-3.9}$		
χ^2_{pos}		0.53			1.29			0.50			1.19		
χ^2_{plim}		0.00			1.17			0.01			1.06		
$\chi^2_{\mathrm{tot}}(N_{\mathrm{dof}})$		**0.53 (2)**			**2.46(2)**			**0.51(0)**			**2.25(0)**		

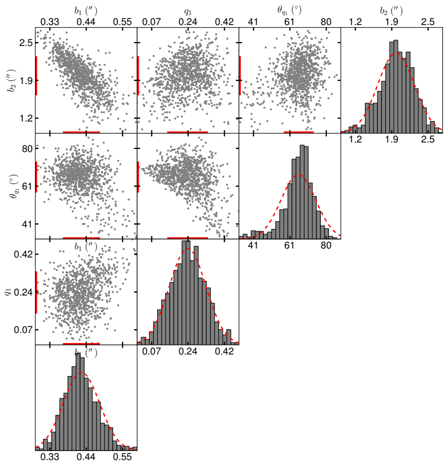

Figure 4.1.4: The free parameters for the model $2SIE_2$ with 6 free parameters, obtained through BS.

parameter limits are imposed on q_1 and θ_{q_1} are more representative of our system, when compared to the luminosity profile.

From Table 4.2, it can be seen that the best models are the second and the fourth ones, where parameter limits are imposed on q_1 and θ_{q_1}, since the BS analysis gives smaller 1σ intervals. The parameter correlations for the best fitting model is shown in Fig. 4.1.4. There is no great improvement shown by allowing q_2 and θ_{q_2} to vary, even with the parameter limits. The χ^2 values goes from 2.46 to 2.25 and therefore the best model in this group of models is the second one. The mass profile of the second model is shown in Fig. 4.1.5. For this model, $M_{\mathrm{G1}}(< \tilde{R}_{\mathrm{E}}) = (3.8 \pm 0.5) \times 10^{10} M_\odot$ which is 58% of $M_{\mathrm{tot}}(< \tilde{R}_{\mathrm{E}})$ and $M_{\mathrm{G2}}(< \tilde{R}_{\mathrm{E}}) = (2.8 \pm 0.5) \times 10^{10} M_\odot$ which is 42% of $M_{\mathrm{tot}}(< \tilde{R}_{\mathrm{E}})$.

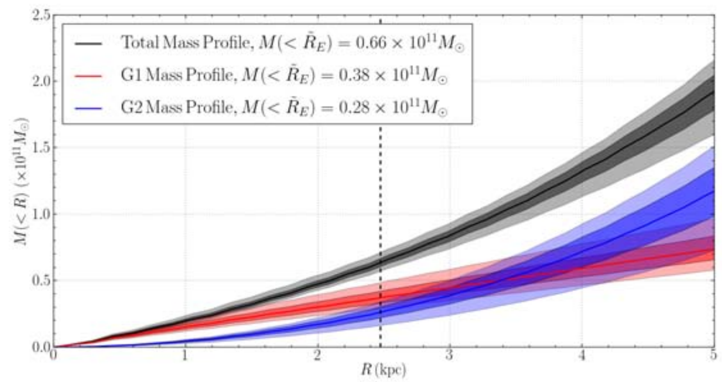

Figure 4.1.5: The mass profile of the best SIE + SIE model, $2\mathrm{SIE}_2$, obtained through BS. The dotted line shows the location of $\tilde{R}_\mathrm{E}$.

SIE + SIS + SIS

Knowing that the galaxies G1 and G2 of this system belong to a galaxy cluster, we investigate the effect of an additional mass component that represents the galaxy cluster. Since G1 is $\sim$ 600 kpc away from the galaxy cluster centre and $\tilde{R}_\mathrm{E} = 2.5$ kpc, the cluster mass contribution can be well approximated with a simple SIS profile. Another option would be to represent the cluster component as an additional shear component but this is not done for two reason:

- We are working with only 8 observables, 2 for each image ($\boldsymbol{x}$), and we would like to keep the number of free parameters of the model to a minimum. Introducing a shear component adds 2 free parameters, the amount of shear and its direction. A single SIS component, at the measured position of the cluster BCG, only adds a single additional free parameter, the lens strength of the cluster component b_c.

- The aim of modelling the lenses is to accurately determine the total mass of G1. This is done by distinguishing the individual mass components from G1, G2 and the cluster at $\tilde{R}_\mathrm{E}$. Shear terms in GRAVLENS are treated as massless components therefore the cluster mass would be "hidden" within the mass of G1 and G2 and add to the overall uncertainty in their estimation.

A SIS profile was added to represent the cluster total mass component and constraints, obtained from a weak lensing study[57], were imposed on b_c. The mass estimate used was $M_{3\mathrm{D}}(r < 1.5\mathrm{Mpc}) = (10.7 \pm 1.4) \times 10^{14} M_\odot$. Using Eq. (1.37), knowing the redshifts of the cluster and of the source and noting that for a 3D mass distribution, $\sigma^2_{\rm SIS} = M_{\rm 3D}G/2R$, we can get an estimate of $b_{\rm SIS} \sim \theta_{\rm E} = (33 \pm 4)''$. When needed, this estimate was used as the parameter limit for b_c during modelling.

To begin with a model where G2 and the cluster were represented as SISs was looked at. This was done to ensure that we would have good starting parameters and a minimum amount of complexity was added at once. For this model we see a significant reduction in the χ^2 value, $\chi^2(N_{\rm dof}) = 0.82(1)$, and the BS analysis gives acceptable 1σ and 2σ values when constraints are imposed on q_1 and θ_{q_1}. The parameters of this model are shown in Table 4.3 and the obtained mass estimates are $M_{\rm G1}(<\tilde{R}_{\rm E}) = (5.0 \pm 0.7) \times 10^{10} M_\odot$ and $M_{\rm G2}(<\tilde{R}_{\rm E}) = (0.5 \pm 0.3) \times 10^{10} M_\odot$, representing 84% and 8% of the total mass budget, respectively. The remaining 8% of the mass is attributed to the cluster.

SIE + SIE + SIS

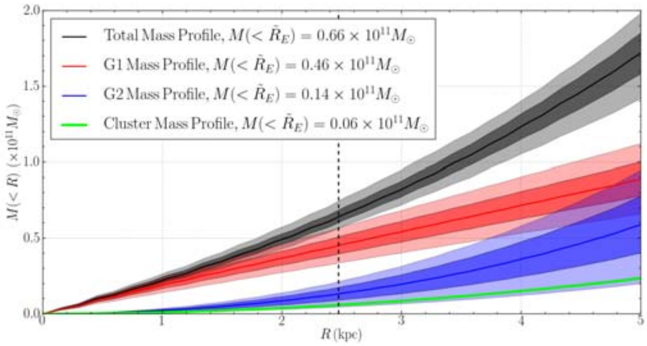

Figure 4.1.6: The mass profile of the best SIE + SIE + SIS model obtained through BS. The dotted line shows the location of $\tilde{R}_{\rm E}$.

Finally, having found that adding the cluster mass component significantly improves our model, as does modelling G2 as a SIE, the last model that was explored comprised of a 2 SIE profiles for G1 and G2 and 1 SIS profile for the cluster mass component. The parameters of this model are b_1, q_1, θ_{q_1}, b_2, q_2, θ_{q2} and b_c. The best model is obtained when constraints are put on q_1, θ_{q1} and b_c. The results for this model are shown in Table 4.3. The χ^2 value, $\chi^2(N_{\rm dof}) = 0.24(1)$, for this model suggests that we are reproducing the multiple image positions very accurately. The parameters of the best fitting model match those obtained through BS analysis with small 1σ values for all of the free parameters. The mass profile obtained from this model is shown in Fig. 4.1.6, with $M_{\rm G1}(<\tilde{R}_{\rm E}) = (4.6 \pm 0.6) \times$

$10^{10} M_\odot$ and $M_{G2}(< \tilde{R}_E) = (1.4 \pm 0.4) \times 10^{10} M_\odot$, representing 70% and 21%, respectively. The remaining 9% of the total mass is attributed to the cluster.. The parameter correlations are shown in Fig. 4.1.7

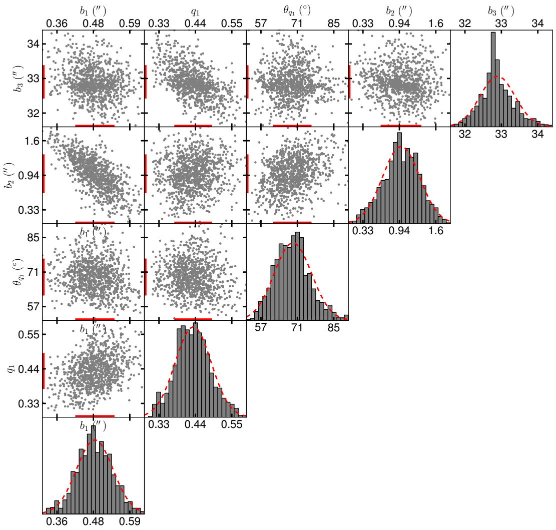

Figure 4.1.7: The parameters of the best SIE + SIE + SIS model obtained through BS analysis.

4.1.3 The systematic error

In order to get an estimate of the systematic error on the total mass of G1, we compare the mass estimates at $\tilde{R}_E$ of the best fitting models. Fig. 4.1.8 shows that the total mass profile of G1 varies by $\sim 40\%$. The statistical error found on the total mass in the earlier sections were $\sim 10\%$, so it is clear that the systematic error dominates the overall error. Other lensing systems typically show a lower total error, $5 - 10\%$ in Koopmans et al. 2006[37] and $\sim 10\%$ in Grillo et al. 2014[28],

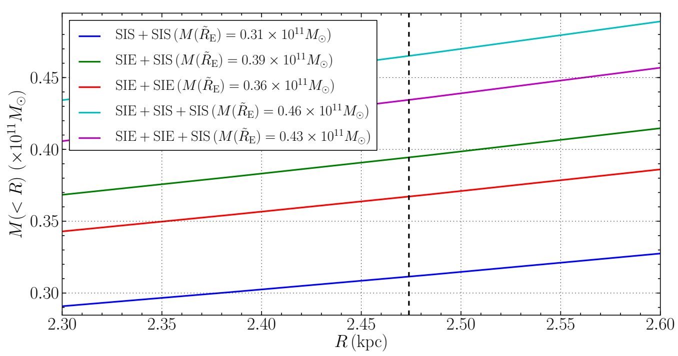

Figure 4.1.8: The total mass profile of G1 for the best models. The dotted line shows the location of $\tilde{R}_E$.

showing that our systematic error is quite high. The systematic error is likely larger here due to the complicated environment in which the main lensing galaxy resides. Not only is there a significant contribution form G2, but the positions of the multiple images are also influenced by the cluster component. One way to reduce this systematic error would be to add independent observations of the velocity dispersions through deep spectroscopy, allowing for additional, independent mass estimates and hence a more accurate estimate of the total projected mass profile of the lenses.

Table 4.3: The optimisation (opt) and the bootstrapping (BS) results for the best models. A ✓ indicates that a parameter is free where as a × indicates that a parameter is fixed.

		SIS + SIS			SIE + SIS			SIE + SIE			SIE + SIS + SIS			SIE + SIE + SIS		
			Free	Limits		Free	Limits		Free	Limits		Free	Limits		Free	Limits
$b_1\,('')$	opt	0.35	✓	-	0.43	✓	-	0.41	✓	-	0.49	✓	-	0.46	✓	-
	BS	$0.39^{+0.05}_{-0.05}$			$0.44^{+0.05}_{-0.05}$			$0.42^{+0.05}_{-0.05}$			$0.51^{+0.07}_{-0.07}$			$0.48^{+0.06}_{-0.05}$		
q_1	opt				0.33	✓	0.4±0.15	0.25	✓	0.4±0.15	0.47	✓	0.4 ± 0.15	0.43	✓	0.4 ± 0.15
	BS				$0.31^{+0.08}_{-0.09}$			$0.24^{+0.09}_{-0.09}$			$0.46^{+0.07}_{-0.05}$			$0.43^{+0.05}_{-0.05}$		
$\theta_{q_1}\,(^\circ)$	opt				69.8	✓	70±15	64.2	✓	70±15	65	✓	70 ± 15	68	✓	70 ± 15
	BS				$70^{+4.1}_{-3.5}$			$0.24^{+0.09}_{-0.09}$			67^{+16}_{-15}			$69^{+6.6}_{-6.6}$		
$b_2\,('')$	opt	0.99	✓	-	1.00	✓	-	2.04	✓	-	1.04	✓	-	1.04	✓	-
	BS	$0.78^{+0.2}_{-0.2}$			$0.97^{+0.17}_{-0.18}$			$1.95^{+0.30}_{-0.30}$			$0.53^{+0.33}_{-0.36}$			$0.97^{+0.31}_{-0.31}$		
q_2	opt							0.80	×	-				0.8	×	-
	BS															
$\theta_{q_2}\,(^\circ)$	opt							-2.0	×	-				-2.0	×	-
	BS															
$b_c\,('')$	opt										29	✓	-	32.8	✓	33 ± 4
	BS										29^{+11}_{-18}			$32.8^{+0.5}_{-0.3}$		
$\chi^2_{\rm pos}$		8.43			2.90			1.29			0.62			0.17		
$\chi^2_{\rm plim}$		0.00			0.22			1.17			0.19			0.07		
$\chi^2_{\rm tot}(N_{\rm dof})$		**8.43(4)**			**3.12(2)**			**2.46(2)**			**0.82(1)**			**0.24(1)**		

Chapter 5

Discussion

5.1 The main lens galaxy, G1

The luminous mass of G1 was measured to be $M_*^{\rm Salp}(<\tilde{R}_{\rm E}) = (2.9 \pm 0.9) \times 10^9 M_\odot$, where the error used was taken to be 30%, a typical error when performing SED fitting. A Salpeter IMF was used, which gives an upper estimate of the luminous mass, with a Chabrier IMF giving a lower mass by a factor ≈ 2. It is still widely debated whether or not the stellar IMF is universal and Salpeter IMF is better than a Chabrier one[10]. A recently submitted paper based on the SLACS survey[55] suggests that a Salpeter IMF results in luminous mass values which are larger than the total ones, obtained through lens modelling when looking at low-mass galaxies, $M_{\rm T}(R_e) < 6.3 \times 10^{10} M_\odot$, where R_e is the galaxy effective radius. Despite this, a Salpeter IMF was used here to give an upper bound to the luminous over total mass fraction, this is discussed in more detail in the next section.

The total mass of G1 for the best fitting lens model was found be $M_{\rm T}(<\tilde{R}_{\rm E}) = (4.6 \pm 0.6) \times 10^{10} M_\odot$ with an additional 40% systematic error. Since the lenses were modelled as having isothermal profiles, the relation

$$M(< R) = \frac{\pi \sigma_v^2 R}{G} \tag{5.1}$$

can be used to estimate the values of an effective velocity dispersion. This is shown in Fig. 5.1.1 for the different models considered in Section 4.1.2. For the best model, a velocity dispersion value of (158 ± 15) km s^{-1} is found. When this velocity dispersion is compared to those of the SLACS galaxies[5], we see

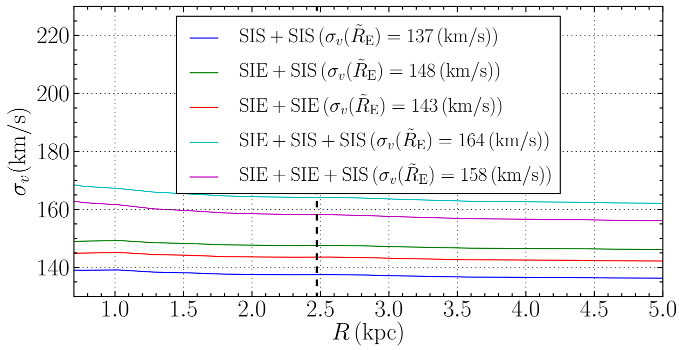

Figure 5.1.1: The velocity dispersion profiles for G1 obtained through lens modelling using the median mass profile found through BS analysis for the 5, best fitting, models chosen.

that it is lower than any of the lenses observed in that survey. High velocity dispersion galaxies were preferentially targeted in the survey, in order to maximise the number of confirmed lenses. Velocity dispersion is correlated with total mass, and therefore, we can infer that our galaxy has a lower mass compared to the galaxies which are commonly found in lens surveys in the field. This provides the opportunity to study a lens galaxy which is in a not well explored mass scale.

Studying a lens in an overdense environment presents some additional complications than modelling an isolated lens galaxy. For example, we found a strong degeneracy between the position angle of G1 and the lens strength of G2. In these complicated systems, it is important to include as many observables as possible in order to better constrain the models and break these degeneracies. A first possibility here would be to include the flux measurements of the multiple images. Including the flux values would give four more observables, allowing us the possibility to explore different power law models for G1 and G2.

Another possibility would be to obtain deep spectroscopic observations in order to measure the stellar velocity dispersion of the lenses. Detailed spectroscopy would give another total mass estimate of the system allowing us to investigate in more detail the properties of G1, G2 and the cluster.

5.2 The luminous over total mass fraction

One of the goals of this thesis was to look at the amount of DM present in the inner regions of the main lens galaxy in order to investigate the relation between luminous and total mass for a low mass galaxy. The values here will be compared to the estimates obtained of two ETGs found close to each other, one of which was of a similar mass to the main lens of this thesis, as discussed by Grillo et al. (2014)[28].

Recent results might suggest that there is a negative correlation between the mass and the luminous over total mass fraction of ETGs[29], defined as

$$f_*(< \tilde{R}_{\mathrm{E}}) = \frac{M_*(< \tilde{R}_{\mathrm{E}})}{M_{\mathrm{T}}(< \tilde{R}_{\mathrm{E}})}, \tag{5.2}$$

but this has not been explored over a large mass range. The *CLASH* team has begun to investigate whether or not this negative correlation holds true to lower masses[28].

Combining the results that we have obtained thus far, we can contribute to this investigation. An upper estimate of the luminous mass within the Einstein radius is found to be $M_*(< \tilde{R}_{\mathrm{E}}) = (2.9 \pm 0.9) \times 10^9 M_\odot$ and the total mass within the Einstein radius is found to be $M_{\mathrm{T}}(< \tilde{R}_{\mathrm{E}}) = (4.6 \pm 0.6) \times 10^{10} M_\odot$. Combining these results gives us $f_*(< \tilde{R}_{\mathrm{E}}) = 0.063 \pm 0.021$. Looking at all of the different models, the values of f_* range between 0.063-0.094, suggesting a 40% systematic error. The low mass system found by Grillo et al. (2014) had two lens galaxies with $f_* = 0.51 \pm 0.21$ and $f_* = 0.80 \pm 0.32$ for each of the lenses, with a total luminous mass of $(1.7 \pm 0.7) \times 10^{10} M_\odot$ and $(4.5 \pm 1.8) \times 10^{11} M_\odot$, respectively.

The luminous over total mass fraction found in this system is considerably lower than other comparable systems, of which there are but a few. A recently submitted paper[55] using data from the SLACS survey measured 40 new lower mass lensing galaxies, with the lowest mass galaxy having a total enclosed mass within the Einstein radius of $1.34 \times 10^{10} M_\odot$. The authors concluded that using a Salpeter IMF to estimate the luminous mass of the galaxies with a total mass less than $6.3 \times 10^{10} M_\odot$, or velocity dispersions smaller than 180 km s^{-1}, resulted in negative DM fractions, where $f_{\mathrm{DM}} := 1 - f_*$. Further considerations should be taken to model the galaxies studied in this thesis to investigate whether or not the luminous over total mass fraction that was found is in fact representative of the main lens. These results infer the following possibilities:

- If this is the true value of f_*, G1 is a DM dominated galaxy to an extent which does not agree with our current understanding. If such systems exist, a statistical analysis of a large enough sample size of lenses would confirm this.

- There could have been an underestimate of the total luminous mass due to the blending of the light between G1 and the multiple images of the source. This could be investigated by observing the system for longer and obtaining a better signal to noise ratio in all of the filter bands.

- The luminous profile that was estimated might be overly steep at small radii, making an overly dense core. The luminous mass is therefore under-represented at the Einstein radius.

- There might been an overestimate of the total mass from lens modelling. One could further investigate this by adding additional observables to the models, such as the flux values of the multiple images, and therefore allow for further constraints on the masses of G1, G2 and the cluster.

The system studied had an unexpectedly low luminous over total mass fraction which is begging to be further explored. There is an approved proposal for deep spectroscopic data on this system which will allow a measurement of the velocity dispersion of the main lens. Should the results of this further research show that the luminous over total mass fraction is indeed what has been estimated in this thesis then this galaxy will be atypical of the currently observed lenses at this mass scale.

Chapter 6

Conclusion

Strong lensing has allowed for precise measurements of the total mass of galaxies, requiring accurate photometric and spectroscopic data. The photometric data is used to measure the positions of a lens and the surrounding multiple images of a more distant source. The spectroscopic data allows us to measure distances between observer and lens, lens and source, and observer and source. These distances characterise the geometry of the whole lensing system.

To date, strong lensing surveys have been used to measure the total mass of hundreds of galaxies[6, 46], in an attempt to better understand the role of DM in galaxy formation and evolution. These surveys have mainly investigated high mass ETGs due of the selection criterion employed: large velocity dispersions. These lensing systems have been well studied, but they are not representative of all galaxies at all mass scales. It is therefore as of yet unclear the extent that DM influences the formation and evolution of low-mass galaxies.

One method of exploring low-mass galaxies is to study those which reside in overdense environments, such as those found in galaxy clusters. These environments not only increase the probability that a source would be lensed into multiple images, but also allow us to probe the properties of the environment.

This thesis has outlined the necessary steps to estimate the total mass of a low-mass lens galaxy located in a galaxy cluster. The observed system consisted of two lensing galaxies, with four multiple images of a single, more distant source. The conclusions of this thesis are thus:

- The lensing models reproduce the observed positions of the multiple images accurately, $\chi^2(N_{\rm dof}) = 0.24(1)$. The best model is found using an SIE profile for G1 and G2 and an SIS profile for the cluster component.

- From a bootstrapping analysis of the best strong lensing model, the total mass of G1 within the Einstein radius is found to be $(4.6 \pm 0.6) \times 10^{10} M_{\odot}$, at a 1σ confidence level.

- A comparison of the different lensing models reproducing well the observables of the system suggests a systematic error of 40%.

- By scaling the stellar mass of G1, obtained through SED fitting in the 5 Subaru bands available, to the luminosity distribution, estimated from *HST/ACS* photometry of a multi-filter image, an upper bound to the luminous mass value at the Einstein radius is found to be $(2.9 \pm 0.9) \times 10^{9} M_{\odot}$. The upper bound is obtained by using simple SSP models and a Salpeter stellar IMF.

- An upper limit to the luminous over total mass fraction of G1 is found to be $f_*(< \tilde{R}_{\rm E}) = 0.063 \pm 0.021$.

A more complete description of the system can be achieved by expanding the analysis to also include G2 and the cluster. The information obtainable for G2 is the same as that for G1: an estimate of the total mass, luminous mass and DM fraction at its Einstein radius. Since the lensing properties of the system are constrained by the positions of the multiple images, and these images are found around G1, the expected error on the total mass estimate of G2 is likely to be larger.

The ability of the lens modelling to characterise the cluster was not explored here due to the low number of observables, 8, and the number of free parameters used in order to reproduce the observed positions of the multiple images of the source. Expanding the observations to also include flux data of the multiple images would give 4 more observables and allow us to further constrain our model and explore in more detail the properties of the cluster. This could also increase the accuracy of our mass estimates, especially for that of G2 since it seemed to be more degenerate with the lens strength of the cluster than G1 was.

Studying these systems is an important step in understanding the distribution of DM and its influence on the formation and evolution of ETGs. Considering that DM constitutes $\sim 20\%$ of the energy budget of the entire Universe, it is important to understand its fundamental properties. Particle physics will contribute by looking for candidates for DM, and astrophysicists will continue to to map DM at different length and mass scales.

Acknowledgements

I would like to thank: my day to day supervisor Claudio Grillo for being very patient with me, igniting my interest in strong gravitational lensing and providing me with a great deal of support not only on the thesis but also on my future academic career; Lise Christensen for giving me the possibility of completing this thesis within the Dark Cosmology Centre and for her input on the photometric and spectroscopic aspects of this thesis; the *CLASH* team for their continued exploration of galaxy clusters and for providing the high quality data used in this thesis; Maria Vistrup Madsen for supporting me during the inevitably stressful last month of writing; Thomas Parry Ford for endeavouring to proof read this thesis; my family, for getting me this far; and everyone at the Dark Cosmology Centre for their enthusiasm in the field of astrophysics.

Appendix

A.1 Derivation of the total luminosity

$$
\begin{aligned}
L &= \int_0^\infty I(R')2\pi R' \mathrm{d}R' \\
I(R) &= I_e \exp\left\{-b_n\left[\left(\frac{R}{R_e}\right)^{\frac{1}{n}} - 1\right]\right\} = I_e \exp\left[-b_n\left(\frac{R}{R_e}\right)^{\frac{1}{n}}\right]\exp(b_n) \\
\Rightarrow L &= 2\pi I_e \exp(b_n)\int_0^\infty R \exp\left[-b_n\left(\frac{R}{R_e}\right)^{\frac{1}{n}}\right]\mathrm{d}R
\end{aligned}
$$

Using the Gamma Function

$$
\Gamma(2n) = \int_0^\infty x^{2n-1}e^{-x} = (2n-1)! \qquad \text{with } x = b_n\left(\frac{R}{R_e}\right)^{\frac{1}{n}}
$$

$$
\Rightarrow L = 2\pi I_e e^{b_n}\frac{n(2n-1)!R_e^2}{(b_n)^{2n}}
$$

Bibliography

[1] S. Arnouts and O. Ilbert. *Le PHARE - PHotometric Analysis for Redshift Estimations*. 2011.

[2] J.-P. Beaulieu et al. “Discovery of a cool planet of 5.5 Earth masses through gravitational microlensing”. In: *Nature* 439 (Jan. 2006), pp. 437–440. DOI: 10.1038/nature04441. eprint: astro-ph/0601563.

[3] G. Bertin. *Dynamics of Galaxies*. Cambridge University Press, 2000. ISBN: 9780521478557.

[4] G. Bertin, L. Ciotti, and M. Del Principe. “Weak homology of elliptical galaxies.” In: *Astronomy & Astrophysics* 386 (Apr. 2002), pp. 149–168. DOI: 10.1051/0004-6361:20020248. eprint: astro-ph/0202208.

[5] A. S. Bolton et al. “The Sloan Lens ACS Survey. I. A Large Spectroscopically Selected Sample of Massive Early-Type Lens Galaxies”. In: *The Astrophysical Journal* 638 (Feb. 2006), pp. 703–724. DOI: 10.1086/498884. eprint: astro-ph/0511453.

[6] A. S. Bolton et al. “The Sloan Lens ACS Survey. V. The Full ACS Strong-Lens Sample”. In: *The Astrophysical Journal* 682 (Aug. 2008), pp. 964–984. DOI: 10.1086/589327. arXiv:0805.1931.

[7] G. Bruzual and S. Charlot. “Stellar population synthesis at the resolution of 2003”. In: *Monthly Notices of the Royal Astronomical Society* 344 (Oct. 2003), pp. 1000–1028. DOI: 10.1046/j.1365-8711.2003.06897.x. eprint: astro-ph/0309134.

[8] D. Calzetti, A. L. Kinney, and T. Storchi-Bergmann. “Dust extinction of the stellar continua in starburst galaxies: The ultraviolet and optical extinction

law". In: *The Astrophysical Journal* 429 (July 1994), pp. 582–601. DOI: 10.1086/174346.

[9] R. G. Carlberg, H. K. C. Yee, and E. Ellingson. "Lensing from the light-traces-mass map of MS 1224+20". In: *The Astrophysical Journal* 437 (Dec. 1994), pp. 63–66. DOI: 10.1086/174975. eprint: astro-ph/9402036.

[10] G. Chabrier. "Galactic Stellar and Substellar Initial Mass Function". In: *Publications of the Astronomical Society of the Pacific* 115 (July 2003), pp. 763–795. DOI: 10.1086/376392. eprint: astro-ph/0304382.

[11] S. Charlot and A. G. Bruzual. "Stellar population synthesis revisited". In: *The Astrophysical Journal* 367 (Jan. 1991), pp. 126–140. DOI: 10.1086/169608.

[12] L. Ciotti. "Stellar systems following the R exp 1/m luminosity law". In: *Astronomy & Astrophysics* 249 (Sept. 1991), pp. 99–106.

[13] S. Courteau et al. "Galaxy masses". In: *Rev. Mod. Phys.* 86 (1 Jan. 2014), pp. 47–119. DOI: 10.1103/RevModPhys.86.47.

[14] G. de Vaucouleurs. "Recherches sur les Nebuleuses Extragalactiques". In: *Annales d'Astrophysique* 11 (Jan. 1948), p. 247.

[15] A. Dressler. "The Dn-sigma relation for bulges of disk galaxies - A new, independent measure of the Hubble constant". In: *The Astrophysical Journal* 317 (June 1987), pp. 1–10. DOI: 10.1086/165251.

[16] A. Dressler et al. "Spectroscopy and photometry of elliptical galaxies. I - A new distance estimator". In: *The Astrophysical Journal* 313 (Feb. 1987), pp. 42–58. DOI: 10.1086/164947.

[17] B. Efron and R.J. Tibshirani. *An Introduction to the Bootstrap*. Chapman & Hall/CRC Monographs on Statistics & Applied Probability. Taylor & Francis, 1994. ISBN: 9780412042317.

[18] A. Einstein. "Die Grundlage der allgemeinen Relativitätstheorie [AdP 49, 769 (1916)]". In: *Annalen der Physik* 517 (Feb. 2005), pp. 517–571. DOI: 10.1002/andp.200590044.

[19] A. Einstein. "Lens-Like Action of a Star by the Deviation og Light in the Gravitational Field". In: *Science* 84.2188 (1936), pp. 506–507. DOI: `10.1126/science.84.2188.506`. eprint: `\url{http://www.sciencemag.org/content/84/2188/506.full.pdf}`.

[20] N. W. Evans and M. I. Wilkinson. "Lens models with density cusps". In: *Monthly Notices of the Royal Astronomical Society* 296 (June 1998), pp. 800–812. DOI: `10.1046/j.1365-8711.1998.01380.x`.

[21] S. M. Faber and R. E. Jackson. "Velocity dispersions and mass-to-light ratios for elliptical galaxies". In: *The Astrophysical Journal* 204 (Mar. 1976), pp. 668–683. DOI: `10.1086/154215`.

[22] G. Fahlman et al. "Dark matter in MS 1224 from distortion of background galaxies". In: *The Astrophysical Journal* 437 (Dec. 1994), pp. 56–62. DOI: `10.1086/174974`. eprint: `astro-ph/9402017`.

[23] W. Forman et al. "X-ray observations of galaxies in the Virgo cluster". In: *The Astrophysical Journal, Letters* 234 (Nov. 1979), pp. L27–L31. DOI: `10.1086/183103`.

[24] W. L. Freedman et al. "Final Results from the Hubble Space Telescope Key Project to Measure the Hubble Constant". In: *The Astrophysical Journal* 553 (May 2001), pp. 47–72. DOI: `10.1086/320638`. eprint: `astro-ph/0012376`.

[25] A. Friedmann. "Über die Krümmung des Raumes". In: *Zeitschrift fur Physik* 10 (1922), pp. 377–386. DOI: `10.1007/BF01332580`.

[26] R. Gavazzi et al. "The Sloan Lens ACS Survey. IV. The Mass Density Profile of Early-Type Galaxies out to 100 Effective Radii". In: *The Astrophysical Journal* 667 (Sept. 2007), pp. 176–190. DOI: `10.1086/519237`. eprint: `astro-ph/0701589`.

[27] C. Grillo. "Elliptical Galaxies as Strong Gravitational Lenses". PhD thesis. Università Degli Studi di Milano, 2007.

[28] C. Grillo et al. "CLASH: Extending Galaxy Strong Lensing to Small Physical Scales with Distant Sources Highly Magnified by Galaxy Cluster Members". In: *The Astrophysical Journal* 786, 11 (May 2014), p. 11. DOI: `10.1088/0004-637X/786/1/11`. arXiv:`1403.0573 [astro-ph.CO]`.

[29] C. Grillo et al. "Photometric mass and mass decomposition in early-type lens galaxies". In: *Astronomy & Astrophysics* 501 (July 2009), pp. 461–474. DOI: 10.1051/0004-6361/200811604. arXiv:0904.3282 [astro-ph.GA].

[30] D. H. Gudehus. "Systematic bias in cluster galaxy data, affecting galaxy distances and evolutionary history". In: *The Astrophysical Journal* 382 (Nov. 1991), pp. 1–18. DOI: 10.1086/170687.

[31] D. Huterer, C. R. Keeton, and C.-P. Ma. "Effects of Ellipticity and Shear on Gravitational Lens Statistics". In: *The Astrophysical Journal* 624 (May 2005), pp. 34–45. DOI: 10.1086/429153. eprint: astro-ph/0405040.

[32] C. R. Keeton. "A Catalog of Mass Models for Gravitational Lensing". In: *ArXiv Astrophysics e-prints* (Feb. 2001). eprint: astro-ph/0102341.

[33] C. R. Keeton. "Computational Methods for Gravitational Lensing". In: *ArXiv Astrophysics e-prints* (Feb. 2001). eprint: astro-ph/0102340.

[34] C. R. Keeton. *gravlens 1.06 - Software for Gravitational Lensing*. 2004.

[35] G. R. Knapp and M. P. Rupen. "Molecular Gas in Elliptical Galaxies: CO Observations of an IRAS Flux-limited Sample". In: *The Astrophysical Journal* 460 (Mar. 1996), p. 271. DOI: 10.1086/176967.

[36] G. R. Knapp, E. L. Turner, and P. E. Cunniffe. "The statistical distribution of the neutral-hydrogen content of elliptical galaxies". In: *The Astronomical Journal* 90 (Mar. 1985), pp. 454–468. DOI: 10.1086/113751.

[37] L. V. E. Koopmans et al. "The Sloan Lens ACS Survey. III. The Structure and Formation of Early-Type Galaxies and Their Evolution since $z \sim 1$". In: *The Astrophysical Journal* 649 (Oct. 2006), pp. 599–615. DOI: 10.1086/505696. eprint: astro-ph/0601628.

[38] J. Kormendy and S. Djorgovski. "Surface photometry and the structure of elliptical galaxies". In: *Annual Review of Astronomy & Astrophysics* 27 (1989), pp. 235–277. DOI: 10.1146/annurev.aa.27.090189.001315.

[39] G. Lemaître. "L'Univers en expansion". In: *Annales de la Société Scientifique de Bruxelles* 53 (1933), p. 51.

[40] The University of Michigan Astronomy Department. *https://dept.astro.lsa.umich.edu*.

[41] B. Moore et al. “Resolving the Structure of Cold Dark Matter Halos”. In: *The Astrophysical Journal, Letters* 499 (May 1998), pp. L5–L8. DOI: 10.1086/311333. eprint: astro-ph/9709051.

[42] A. B. Newman et al. “The Density Profiles of Massive, Relaxed Galaxy Clusters. I. The Total Density Over Three Decades in Radius”. In: *The Astrophysical Journal* 765, 24 (Mar. 2013), p. 24. DOI: 10.1088/0004-637X/765/1/24. arXiv:1209.1391 [astro-ph.CO].

[43] A. B. Newman et al. “The Density Profiles of Massive, Relaxed Galaxy Clusters. II. Separating Luminous and Dark Matter in Cluster Cores”. In: *The Astrophysical Journal* 765, 25 (Mar. 2013), p. 25. DOI: 10.1088/0004-637X/765/1/25. arXiv:1209.1392 [astro-ph.CO].

[44] C. Y. Peng. *Galfit User's Manual.* 2003.

[45] M. M. Phillips et al. “Ionized gas in elliptical and S0 galaxies. I - A survey for H-alpha and forbidden N II emission”. In: *The Astronomical Journal* 91 (May 1986), pp. 1062–1085. DOI: 10.1086/114083.

[46] M. Postman et al. “The Cluster Lensing and Supernova Survey with Hubble: An Overview”. In: *The Astrophysical Journal, Supplement* 199, 25 (Apr. 2012), p. 25. DOI: 10.1088/0067-0049/199/2/25. arXiv:1106.3328 [astro-ph.CO].

[47] H. P. Robertson. “Kinematics and World-Structure”. In: *The Astrophysical Journal* 82 (Nov. 1935), p. 284. DOI: 10.1086/143681.

[48] V. C. Rubin. “The rotation of spiral galaxies”. In: *Science* 220 (June 1983), pp. 1339–1344. DOI: 10.1126/science.220.4604.1339.

[49] E. E. Salpeter. “The Luminosity Function and Stellar Evolution.” In: *The Astrophysical Journal* 121 (Jan. 1955), p. 161. DOI: 10.1086/145971.

[50] V. Salzano et al. “Improving dark energy constraints with high-redshift Type Ia supernovae from CANDELS and CLASH”. In: *Astronomy & Astrophysics* 557, A64 (Sept. 2013), A64. DOI: 10.1051/0004-6361/201321738. arXiv:1307.0820 [astro-ph.CO].

[51] P. Schneider. *Extragalactic Astronomy and Cosmology: An Introduction.* Springer, 2006. ISBN: 9783540331742.

[52] P. Schneider, J. Ehlers, and E.E. Falco. *Gravitational Lenses*. Astronomy and Astrophysics Library. Springer, 1999. ISBN: 9783540665069.

[53] P. Schneider et al. *Gravitational Lensing: Strong, Weak and Micro: Saas-Fee Advanced Course 33*. Saas-Fee Advanced Course. Springer Berlin Heidelberg, 2010. ISBN: 9783642067778.

[54] J. L. Sérsic. "Influence of the atmospheric and instrumental dispersion on the brightness distribution in a galaxy". In: *Boletin de la Asociacion Argentina de Astronomia La Plata Argentina* 6 (1963), p. 41.

[55] Y. Shu et al. "The Sloan Lens ACS Survey. XII. Extending Strong Lensing to Lower Masses". In: *ArXiv e-prints* (July 2014). arXiv:1407.2240.

[56] S. H. Suyu et al. "Two Accurate Time-delay Distances from Strong Lensing: Implications for Cosmology". In: *The Astrophysical Journal* 766, 70 (Apr. 2013), p. 70. DOI: 10.1088/0004-637X/766/2/70. arXiv:1208.6010 [astro-ph.CO].

[57] K. Umetsu et al. "CLASH: Weak-Lensing Shear-and-Magnification Analysis of 20 Galaxy Clusters". In: *ArXiv e-prints* (Apr. 2014). arXiv:1404.1375.

[58] A. G. Walker and E. A. Milne. "On the Formal Comparison of Milne's Kinematical System with the Systems of General Relativity". In: *Monthly Notices of the Royal Astronomical Society* 95.3 (1935), pp. 263–269. DOI: 10.1093/mnras/95.3.263. eprint: \url{http://mnras.oxfordjournals.org/content/95/3/263.full.pdf+html}.

[59] D. Walsh, R. F. Carswell, and R. J. Weymann. "0957 + 561 A, B: twin quasistellar objects or gravitational lens?" In: *Nature* 279.5712 (1979), pp. 381–384.

[60] A. Wirth and J. S. Gallagher III. "The families of elliptical-like galaxies". In: *The Astrophysical Journal* 282 (July 1984), pp. 85–94. DOI: 10.1086/162178.

[61] W. Zheng et al. "A magnified young galaxy from about 500 million years after the Big Bang". In: *Nature* 489 (Sept. 2012), pp. 406–408. DOI: 10.1038/nature11446. arXiv:1204.2305 [astro-ph.CO].

[62] A. Zitrin et al. "CLASH: Discovery of a Bright z ˜= 6.2 Dwarf Galaxy Quadruply Lensed by MACS J0329.6-0211". In: *The Astrophysical Journal, Letters* 747, L9 (Mar. 2012), p. L9. DOI: 10.1088/2041-8205/747/1/L9. arXiv:1111.5006 [astro-ph.CO].

[63] A. Zocchi, G. Bertin, and A. L. Varri. "A dynamical study of Galactic globular clusters under different relaxation conditions". In: *Astronomy & Astrophysics* 539, A65 (Mar. 2012), A65. DOI: 10.1051/0004-6361/201117977. arXiv:1201.1466 [astro-ph.GA].

[64] F. Zwicky. "On the Masses of Nebulae and of Clusters of Nebulae". In: *The Astrophysical Journal* 86 (Oct. 1937), p. 217. DOI: 10.1086/143864.